

Discovery and Rapid Follow-up Observations of the Unusual Type II SN 2018ivc in NGC 1068

```
K. A. Bostroem<sup>1</sup>, S. Valenti<sup>1</sup>, D. J. Sand<sup>2</sup>, J. E. Andrews<sup>2</sup>, S. D. Van Dyk<sup>3</sup>, L. Galbany<sup>4</sup>, D. Pooley<sup>5,6</sup>, R. C. Amaro<sup>2</sup>, N. Smith<sup>2</sup>, S. Yang<sup>1,7,8</sup>, G. C. Anupama<sup>9</sup>, I. Arcavi<sup>10,11</sup>, E. Baron<sup>12</sup>, P. J. Brown<sup>13</sup>, J. Burke<sup>14,15</sup>, R. Cartier<sup>16</sup>, D. Hiramatsu<sup>14,15</sup>, R. Dastidar<sup>17,18</sup>, J. M. DerKacy<sup>12</sup>, Y. Dong<sup>1</sup>, E. Egami<sup>2</sup>, S. Ertel<sup>2,19</sup>, A. V. Filippenko<sup>20,36</sup>, O. D. Fox<sup>21</sup>, J. Haislip<sup>22</sup>, G. Hosseinzadeh<sup>23</sup>, D. A. Howell<sup>14,15</sup>, A. Gangopadhyay<sup>17,24</sup>,
     S. W. Jha<sup>25</sup>, V. Kouprianov<sup>22,26</sup>, B. Kumar<sup>9</sup>, M. Lundquist<sup>2</sup>, D. Milisavljevic<sup>27</sup>, C. McCully<sup>14,15</sup>, P. Milne<sup>2</sup>, K. Misra<sup>1,17</sup>, D. E. Reichart<sup>22</sup>, D. K. Sahu<sup>9</sup>, H. Sai<sup>28</sup>, A. Singh<sup>9,29</sup>, P. S. Smith<sup>2</sup>, J. Vinko<sup>30,31</sup>, X. Wang<sup>28</sup>, Y. Wang<sup>32</sup>, J. C. Wheeler<sup>31</sup>, G. G. Williams<sup>2,33</sup>, S. Wyatt<sup>2</sup>, J. Zhang<sup>34,35</sup>, and X. Zhang<sup>28</sup>
                          Department of Physics, University of California, 1 Shields Avenue, Davis, CA 95616-5270, USA; kabostroem@ucdavis.edu

Steward Observatory, University of Arizona, 933 North Cherry Avenue, Tucson, AZ 85721-0065, USA

Caltech/IPAC, Mailcode 100-22, Pasadena, CA 91125, USA
                                             <sup>4</sup> Departamento de Fsica Terica y del Cosmos, Universidad de Granada, E-18071 Granada, Spain
                                                        Department of Physics and Astronomy, Trinity University, San Antonio TX, USA

<sup>6</sup> Eureka Scientific, Inc., USA
                       <sup>7</sup> Department of Physics and Astronomy Galileo Galilei, University of Padova, Vicolo dell'Osservatorio, 3, I-35122 Padova, Italy
                                               INAF—Osservatorio Astronomico di Padova, Vicolo dell'Osservatorio 5, I-35122 Padova, Italy
                                                      Indian Institute of Astrophysics, Koramangala 2nd Block, Bengaluru 560 034, India
                                                    10 The School of Physics and Astronomy, Tel Aviv University, Tel Aviv 69978, Israel
                                                                   CIFAR Azrieli Global Scholars program, CIFAR, Toronto, Canada
                                       <sup>12</sup> Homer L. Dodge Department of Physics and Astronomy, University of Oklahoma, Norman, OK, USA
                             13 Mitchell Institute for Fundamental Physics and Astronomy, Texas A&M University, College Station, TX 77843, USA
                                                     Department of Physics, University of California, Santa Barbara, CA 93106-9530, USA
                                                15 Las Cumbres Observatory, 6740 Cortona Drive, Suite 102, Goleta, CA 93117-5575, USA
                                <sup>16</sup> Cerro Tololo Inter-American Observatory, National Optical Astronomy Observatory, Casilla 603, La Serena, Chile
                                                 Aryabhatta Research Institute of observational sciences, Manora Peak, Nainital 263 001, India
                                                         Department of Physics & Astrophysics, University of Delhi, Delhi-110 007, India
                                                 <sup>19</sup> Large Binocular Telescope Observatory, 933 North Cherry Avenue, Tucson, AZ 85721, USA
                                                      Department of Astronomy, University of California, Berkeley, CA 94720-3411, USA
                                                 <sup>21</sup> Space Telescope Science Institute, 3700 San Martin Drive, Baltimore, MD 21218, USA
                               <sup>22</sup> Department of Physics and Astronomy, University of North Carolina at Chapel Hill, Chapel Hill, NC 27599, USA
             Center for Astrophysics | Harvard & Smithsonian, 60 Garden Street, Cambridge, MA 02138-1516, USA

24 Pt. Ravi Shankar Shukla University, Raipur 492 010, India

Department of Physics and Astronomy, Rutgers, the State University of New Jersey, 136 Frelinghuysen Road, Piscataway, NJ 08854, USA
                           Central (Pulkovo) Observatory of Russian Academy of Sciences, 196140 Pulkovskoye Avenue 65/1, Saint Petersburg, Russia
                               Department of Physics and Astronomy, Purdue University, 525 Northwestern Avenue, West Lafayette, IN. 47907, USA
                 <sup>28</sup> Physics Department and Tsinghua Center for Astrophysics (THCA), Tsinghua University, Beijing, 100084, People's Republic of China
                                        Joint Astronomy Programme, Department of Physics, Indian Institute of Science, Bengaluru 560012, India
                <sup>30</sup> Konkoly Observatory, Research Centre for Astronomy and Earth Sciences, Hungarian Academy of Sciences, H-1121 Budapest, Hungary Department of Astronomy, University of Texas at Austin, Austin, TX 78712, USA
     32 Key laboratory of Optical Astronomy, National Astronomical Observatories, Chinese Academy of Sciences, Beijing, 100101, People's Republic of China
                                                    <sup>3</sup> MMT Observatory, P.O. Box 210065, University of Arizona, Tucson, AZ 85721, USA
                                        <sup>34</sup> Yunnan Observatories, Chinese Academy of Sciences, Kunming 650216, People's Republic of China
         35 Key Laboratory for the Structure and Evolution of Celestial Objects, Chinese Academy of Sciences, Kunming 650216, People's Republic of China
                                           Received 2019 September 16; revised 2020 April 6; accepted 2020 April 7; published 2020 May 21
```

Abstract

We present the discovery and high-cadence follow-up observations of SN 2018ivc, an unusual SNe II that exploded in NGC 1068 (D=10.1 Mpc). The light curve of SN 2018ivc declines piecewise-linearly, changing slope frequently, with four clear slope changes in the first 30 days of evolution. This rapidly changing light curve indicates that interaction between the circumstellar material and ejecta plays a significant role in the evolution. Circumstellar interaction is further supported by a strong X-ray detection. The spectra are rapidly evolving and dominated by hydrogen, helium, and calcium emission lines. We identify a rare high-velocity emission-line feature blueshifted at ~7800 km s⁻¹ (in H α , H β , P β , P γ , He I, and Ca II), which is visible from day 18 until at least day 78 and could be evidence of an asymmetric progenitor or explosion. From the overall similarity between SN 2018ivc and SN 1996al, the H α equivalent width of its parent H II region, and constraints from pre-explosion archival Hubble Space Telescope images, we find that the progenitor of SN 2018ivc could be as massive as 52 M_{\odot} but is more likely <12 M_{\odot} . SN 2018ivc demonstrates the importance of the early discovery and rapid follow-up observations of nearby supernovae to study the physics and progenitors of these cosmic explosions.

³⁶ Miller Senior Fellow, Miller Institute for Basic Research in Science, University of California, Berkeley, CA 94720, USA

Unified Astronomy Thesaurus concepts: Circumstellar gas (238); Core-collapse supernovae (304); Type II supernovae (1731)

Supporting material: animation, machine-readable table

1. Introduction

Single stars with masses greater than $\sim 8 M_{\odot}$ are thought to explode as core-collapse supernovae (SNe). SNe II, those with hydrogen in their spectra, are empirically classified by the shape of their light curves. The light curves of SNe IIP show a long plateau, ~80-120 days after explosion, before falling by a few magnitudes over \sim 20 days and eventually settling on a decline powered by the radioactive decay of $^{56}\mathrm{Ni} \rightarrow$ $^{56}\text{Co} \rightarrow ^{56}\text{Fe}$. On the other hand, the light curves of historical SNe IIL (e.g., SN 1979C, SN 1980K) decline linearly (in mag day⁻¹) before transitioning to the radioactive decay phase. While historically these two classes were separated (e.g., Barbon et al. 1979; Patat et al. 1993, 1994; Arcavi et al. 2012; Faran et al. 2014a, 2014b), today, with larger samples of light curves, we see that these classes blur together: there are intermediate objects showing a linear decline like that of SNe IIL and a clear fall onto the radioactive decay tail like that of SNe IIP (Anderson et al. 2014; Valenti et al. 2015; Galbany et al. 2016b). Additionally, there appears to be a smooth continuum of slopes during the hydrogen recombination phase. Throughout this paper, we will refer to this collective class as SNe IIP/IIL, and we use the Type IIL-like designation to indicate objects that are similar to the historical SNe IIL and Type IIP-like to describe SNe that show a clear plateau.

The continuity of SN IIP/IIL observational properties makes sense when one considers the physical mechanism producing the plateau in Type IIP-like SNe. The progenitors of SNe IIP/ IIL are massive stars with hydrogen envelopes. This hydrogen is ionized by the SN shock, and as it cools, it recombines, producing a receding recombination front in the expanding ejecta. The progenitors of Type IIP-like SNe have large hydrogen envelopes and a recession rate that matches the expansion rate, producing a constant luminosity. If the progenitor has experienced more mass loss, then the hydrogen envelope is less massive. In this case, the canonical picture is that the photosphere recedes faster, leading to a linearly declining light curve, the steepness of which depends on the amount of hydrogen in the envelope (Grassberg et al. 1971; Young & Branch 1989; Blinnikov & Bartunov 1993; Moriya et al. 2016). We note that although this is the standard explanation, the physical mechanism that produces Type IILlike SNe is not well understood, and it is also possible that increased ⁵⁶Ni mass or interaction with circumstellar material (CSM) could produce a linearly decaying light curve.

Over the course of its lifetime, the material lost via winds from the progenitor star leads to a substantial amount of CSM. The configuration of the CSM and its density depend on the time of the mass loss, the rate of the mass loss (which could be steady or episodic), and the symmetry of the mass loss. Once the star explodes, the radiation, shock wave, and (at later times) ejecta can interact with the material lost prior to explosion, producing observational signatures such as narrow emission lines, enhanced luminosity, and blue colors (Smith 2014). When narrow or intermediate-width hydrogen emission lines are observed, the SN is denoted an SN IIn (see, e.g., Filippenko 1997, for a review of SNe). Historically, CSM was identified in SNe either through narrow lines produced by

unshocked, photoionized CSM, intermediate-width lines created by shocked CSM, or by light curves that deviated from the typical Type IIP/IIL shape and color. Recently, signs of interaction have been identified beyond these traditional diagnostics. CSM interaction has been seen in SNe IIP/IIL at late phases (Andrews et al. 2010; Mauerhan et al. 2017), early CSM interaction has been invoked to explain the early-time light curve of most SNe IIP/IIL (Morozova et al. 2017, 2018), and the presence of CSM material very close to the progenitor has been used to explain early, narrow, high-ionization features ("flash spectroscopy" lines) in several SNe II (e.g., Quimby et al. 2006; Gal-Yam et al. 2014; Smith et al. 2015; Khazov et al. 2016; Hosseinzadeh et al. 2018). Each of these signatures of interaction occurs during a specific phase of evolution and could be missed without continuous and frequent observations from explosion through the nebular phase. In order to fully understand the mass-loss history of their progenitors, it is important to follow SNe IIP/IIL as close to explosion as possible, for as long as possible, with the highest cadence available.

Here, we present observations of SN 2018ivc, a Type IILlike SN that exploded in a complex CSM environment in the well-studied Seyfert 2 galaxy NGC 1068 (M77; see Figure 1), and which was discovered by the $D < 40 \,\mathrm{Mpc}$ SN Survey (DLT40; Tartaglia et al. 2018). We adopt a distance of $D = 10.1 \,\mathrm{Mpc} \ (\mu = 30.02 \,\mathrm{mag}; \,\mathrm{Tully} \,\mathrm{et} \,\mathrm{al.} \,\, 2008)$ and a recessional velocity of $1037 \,\mathrm{km} \,\mathrm{s}^{-1}$ (z = 0.003793; Huchra et al. 1999) for NGC 1068 in this work. Our near-daily observations of the SN show the presence of several rapid changes, both in the spectra and in the light curve, which could be easily missed in undersampled observations of other Type IIL-like SNe. In Section 2 of this paper, we discuss recent improvements to the DLT40 pipeline that enabled the very rapid discovery and follow-up observations of SN 2018ivc. We then describe the photometric and spectroscopic observations in Section 3, determine the properties of SN 2018ivc and its host galaxy in Section 4, and discuss the spectroscopic and photometric evolution of SN 2018ivc in Section 5. In Section 6, we present our search for a progenitor in archival images from the Hubble Space Telescope (HST) and our identification of an SN in the literature with a similar evolution. Properties of the progenitor system are considered in Section 7, and the paper is summarized in Section 8.

2. DLT40 Discovery and Rapid Follow-up Campaigns

2.1. DLT40 Survey and Recent Improvements

We briefly summarize the relevant aspects of the high-cadence DLT40 SN survey, the mechanics of which are described in more detail in Yang et al. (2017, 2019) and Tartaglia et al. (2018). DLT40 is a \sim 12 hr cadence search for SNe, targeting galaxies within $D \lesssim 40$ Mpc, designed with the goal of discovering \sim 10 SNe per year within a day of explosion. Since 2017 December, DLT40 has operated two nearly identical 0.41 m telescopes, one at Cerro Tololo Inter-American Observatory (CTIO) in Chile and the other at Meckering Observatory in Western Australia. Each telescope

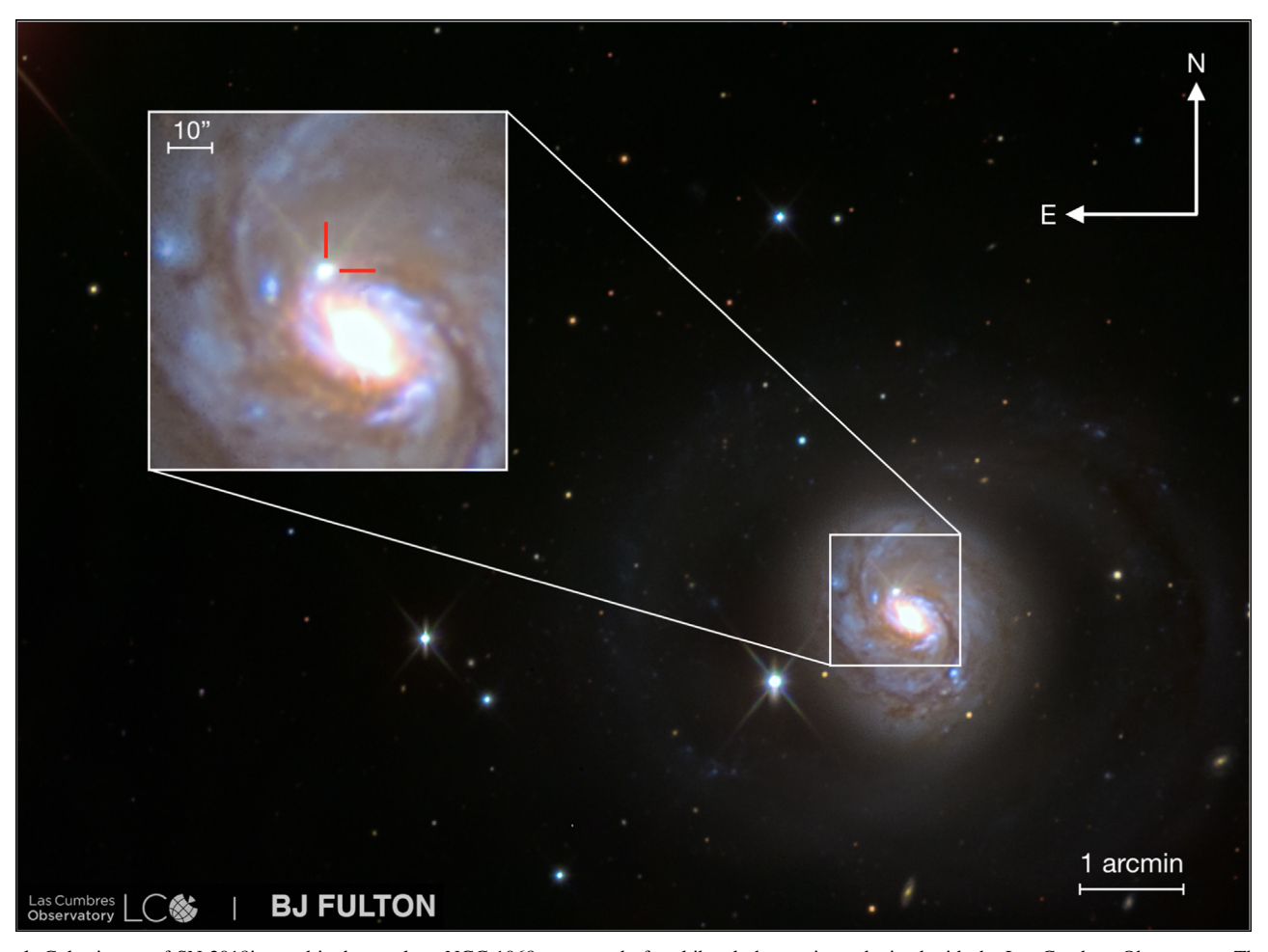


Figure 1. Color image of SN 2018ivc and its host galaxy NGC 1068 composed of multiband observations obtained with the Las Cumbres Observatory. The inset shows a zoomed image of the nuclear region of NGC 1068. SN 2018ivc is indicated with the red guider lines northeast of the nucleus.

strives to observe the same set of \sim 400–600 galaxies each night, providing the effective \sim 12 hr search cadence. The exposure time is 45 s per field, in a clear or open filter, with a typical limiting magnitude of $r \approx 19$ mag in good sky conditions. As we describe below, the search for SNe happens in real time, nearly 24 hr a day.

Several recent improvements to the DLT40 pipeline led to the immediate identification of SN 2018ivc as a true SN, and enabled the rapid follow-up campaign. First, DLT40 SN candidates are scored in real time using a version of the pixelbased, random forest machine-learning algorithm used by the Pan-STARRS1 survey (Wright et al. 2015). Once a new, strong SN candidate is identified by the DLT40 algorithm, an email alert is immediately sent to the team, and a follow-up observation with a DLT40 telescope can be urgently requested at the click of a button to verify the new transient. If the response to the automated email alert is immediate, the entire process from data collection to automated discovery to confirmation imaging takes approximately five minutes and truly brings the follow-up response into real time. Once a new SN has been verified with follow-up imaging, we often trigger a sequence of intranight DLT40 images, which can elucidate rapid light-curve evolution, as was the case for SN 2018ivc. Links in the internal DLT40 web pages allow for nearly automated photometric and spectroscopic triggers of new SNe with the Las Cumbres Observatory network of telescopes (Brown et al. 2013), and we always request a target of opportunity (ToO) sequence of multiband Swift images to probe the early ultraviolet (UV) light-curve evolution. The DLT40 team also announces all verified SN candidates immediately through the Transient Name Service³⁷ (TNS)—there are no proprietary candidates.

2.2. SN 2018ivc Discovery and Rapid Follow-up Observations

The initial DLT40 discovery image of SN 2018ivc (which was given an internal DLT40 designation of DLT18aq) was taken on 2018 November 24.04 (UT dates are used throughout this paper) by the PROMPT5 telescope on CTIO, with a magnitude of $r=14.65\pm0.02$. The DLT40 machine-learning algorithm identified a strong SN candidate in the initial image of the NGC 1068 field, and an email alert was sent out two minutes later. One of us (R.C.A.) quickly inspected the SN candidate on the DLT40 internal website and triggered a second observation, which was taken 14 minutes after the discovery image. Once the SN candidate was confirmed, we took a sequence of PROMPT5 images of the field over the next \sim 2.5 hr, during which the SN brightened from the initial r = 14.65 to 14.61 mag. During this time period, we reported the SN candidate to the community (Valenti et al. 2018) and also triggered the Las Cumbres Observatory network of robotic telescopes to obtain multiband observations (UBVgri) as soon

https://wis-tns.weizmann.ac.il

as possible (first images on 2018 November 24.11, 2 hr after discovery). We obtained our first spectrum with the FLOYDS spectrograph on 2018 November 24.28 and a second spectrum with the BFOSC spectrograph on 2018 November 24.70 (Zhang et al. 2018).

The last non-detection in the NGC 1068 field by the DLT40 team was on 2018 November 19. The field of NGC 1068 had not been observed in the days just prior to the discovery of SN 2018ivc, owing to the lunar angle constraint that DLT40 places on its target fields ($\theta_{\text{Moon}} > 25^{\circ}$).

3. Observations

The photometric and spectroscopic follow-up observations of SN 2018ivc were obtained and coordinated through Las Cumbres Observatory's Global Supernova Project (GSP; PI: D. A. Howell), a key project to collect densely sampled optical light curves and spectra of nearby and bright SNe (e.g., Andrews et al. 2019; Szalai et al. 2019).

In addition to the extensive optical data set, we also obtained early UV and near-infrared (NIR) photometry and NIR spectroscopy throughout the first $\sim\!50$ days as well as an early X-ray observation. ³⁸

3.1. Photometry

Starting within hours of discovery, high-cadence optical photometric data from the Las Cumbres Observatory telescope network were acquired in the <code>UBVgri</code> bands for SN 2018ivc; all data were reduced using the <code>lcogtsnpipe</code> software suite (Valenti et al. 2016) on difference images. Photometric monitoring with the Las Cumbres Observatory was stopped when we were no longer able to detect the SN against the bright host background, on 2019 January 21.18 (day 60). These observations were supplemented with high-cadence photometry from the DLT40 survey, observed with the Open/Clear filters and calibrated to the <code>r</code> band. These observations were reduced using the <code>DLT40 pipeline</code> (Tartaglia et al. 2018), and photometry was performed on difference images. DLT40 monitoring was stopped when the SN disappeared behind the Sun.

We augment these observations with data from the 1.04 m Sampurnanand Telescope in the *BVRI* bands (Sagar 1999), the 1.3 m Devasthal Fast Optical Telescope in the *BVRI* bands (Sagar et al. 2012), the 2.01 m Himalayan Chandra Telescope (HCT) in the *BVRI* bands (Prabhu & Anupama 2010), the Mont4K instrument on the 1.55 m Kuiper Telescope in the *UBV* bands, and the 0.6 m Super-LOTIS telescope (Williams et al. 2008) in the *BVRI* bands. Point-spread-function photometry was performed on the original images using the DAOPhot (Stetson 1987) Pyraf³⁹ package. As the photometry of these observations was not performed on difference images, imperfect background subtraction produces more scatter in the light curves. The optical light curve is presented in Figure 2.

Late-time optical observations were obtained with HST on 2019 July 1 using the Wide Field Camera 3 (WFC3) UVIS channel (F555W and F814W), as part of the ToO program

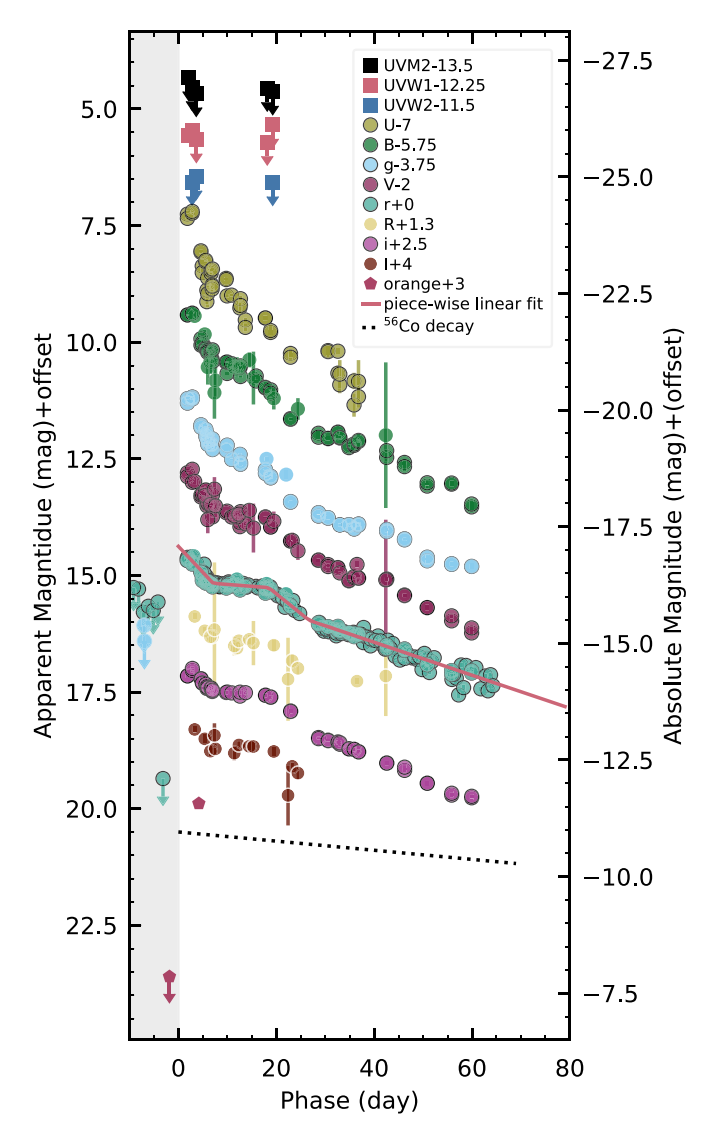


Figure 2. Light curve of SN 2018ivc at UV (square symbols) and optical (circles and pentagons) wavelengths. Difference-image photometry is indicated by the black outlines. The upper limits are denoted with arrows. All phases are calculated with respect to the inferred explosion epoch (2018 November 22.25; see Section 4), and the period prior to this time is shaded in gray. The piecewise linear fit of the DLT40 *r*-band light curve is shown in pink. Individual filters have been offset by a constant (denoted in the legend) for ease of viewing. The black dashed line shows the *V*-band slope expected if the light curve is fully powered by the radioactive decay of ⁵⁶Co.

GO-15151 (PI: S. Van Dyk). We used Dolphot (Dolphin 2000, 2016) to extract the photometry from the FLC frames. A list of all photometric observations is available in the electronic version of Table 1.

SN 2018ivc was also observed with the Neil Gehrels Swift Observatory (Gehrels et al. 2004). Observations with the Ultra-Violet Optical Telescope (UVOT; Roming et al. 2005) were reduced and analyzed using the pipeline for the Swift Optical Ultraviolet Supernova Archive (SOUSA; Brown et al. 2014), which includes an arithmetic subtraction of the underlying host-galaxy flux measured from pre-explosion imaging. The magnitudes use the updated calibration from Breeveld et al. (2010) and are on the UVOT/Vega system. Optical magnitudes are not reported because the underlying host galaxy was too bright to correct for the coincidence loss. Upper limits in *uvw2*

 $[\]overline{^{38}}$ We also obtained Giant Metrewave Radio Telescope observations. However, we found issues with the calibration that rendered the observations unusable.

³⁹ Pyraf is a product of the Space Telescope Science Institute, which is operated by AURA, Inc., for NASA.

 Table 1

 Example of the Photometric Observations of SN 2018ivc

Observation Date UT	MJD	Phase (day)	Source	Filter	Magnitude (mag)	Magnitude Error (mag)
2018 Nov 13 02:16:15.16	58435.09	-9.16	CTIO-Prompt5	Open	<15.26	
2018 Nov 14 02:33:08.64	58436.11	-8.14	CTIO-Prompt5	Open	<15.29	
2018 Nov 15 02:24:00.86	58437.10	-7.15	CTIO-Prompt5	Open	<15.79	
2018 Nov 15 05:56:24.00	58437.25	-7.00	ZTF	g	<19.82	
2018 Nov 15 07:29:16.80	58437.31	-6.94	ZTF	g	< 20.16	
2018 Nov 16 03:03:18.72	58438.13	-6.12	CTIO-Prompt5	Open	<15.66	
2018 Nov 17 02:50:24.57	58439.12	-5.13	CTIO-Prompt5	Open	<15.75	
2018 Nov 18 02:02:48.19	58440.09	-4.16	CTIO-Prompt5	Open	<15.57	
2018 Nov 19 02:39:18.43	58441.11	-3.14	CTIO-Prompt5	Open	<19.36	
2018 Nov 20 10:14:52.00	58442.43	-1.82	ATLAS	o	<18.60	
2018 Nov 24 00:52:16.32	58446.04	1.79	CTIO-Prompt5	Open	14.65	0.01
2018 Nov 24 01:14:37.24	58446.05	1.80	CTIO-Prompt5	Open	14.66	0.01
2018 Nov 24 01:06:45.50	58446.05	1.80	CTIO-Prompt5	Open	14.68	0.01
2018 Nov 24 01:33:23.90	58446.06	1.81	CTIO-Prompt5	Open	14.63	0.01
2018 Nov 24 02:14:47.04	58446.09	1.84	LCO LSC 1 m	U	14.35	0.02

Note. The UVW1, UVW2, UVM2, U, B, and V filters are given in the Vega magnitude system; the g, r, and i filters are given in the AB magnitude system. (This table is available in its entirety in machine-readable form.)

and *uvm2* and detections in *uvw1* are included in Table 1 and plotted in Figure 2.

3.2. Spectroscopy

Spectroscopic observations from a variety of telescopes and instruments were obtained almost daily in the optical, starting within 5 hr of discovery and continuing through day 35. Less-frequent monitoring with larger telescopes was performed until SN 2018ivc disappeared behind the Sun $\sim\!80$ days post-discovery. A single nebular spectrum was obtained with Keck/DEIMOS on day 279 (see Figure 3).

Similarly, NIR observations began on day 3 and continued almost weekly through day 53. A selection of spectra is shown in Figure 4, and all spectroscopic observations are listed in Table A1. All of the spectra presented in this work were obtained at the parallactic angle to minimize atmospheric refraction (Filippenko 1982). These spectra will be made available on WISeREP⁴⁰ (Yaron & Gal-Yam 2012).

Optical spectra were reduced using standard techniques, including bias subtraction, flat-fielding, and cosmic-ray rejection. SN 2018ivc is embedded in NGC 1068; given this complex background, local sky subtraction was very important for the spectral extraction. Despite the care taken, some narrow emission lines are still visible in the final reduced spectra. In these cases, after visual inspection of two-dimensional spectra and our highest-resolution data (see Section 5.2 for a detailed discussion), we believe these originate from the host galaxy.

Flux calibration was performed using standard-star observations. For the NIR spectra, the data were reduced in a similar manner as by Hsiao et al. (2019), using the standard ABBA technique; observations were taken of nearby A0V stars adjacent to the science exposures to facilitate telluric corrections and flux calibration (e.g., Vacca et al. 2003).

3.3. X-Ray Observations

The Chandra X-ray Observatory observed SN 2018ivc on 2018 December 05.7 for 10.0 ks (ObsID 20306) with the



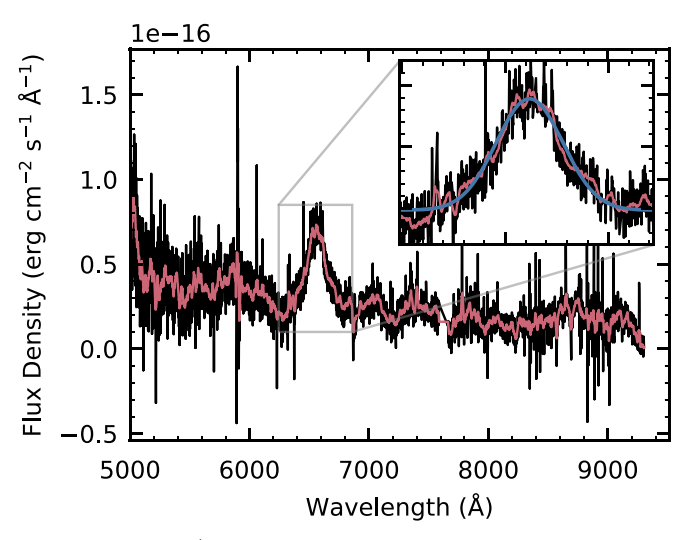


Figure 3. The Keck/DEIMOS nebular spectrum, observed on day 279 (in black; pink represents smoothed by 25 pixels) with a zoom-in on the $H\alpha$ region in the inset. A single Gaussian fit is shown in the inset in blue. Although the spectrum has a low signal-to-noise ratio (S/N), there is no evidence of multiple components in the $H\alpha$ feature.

telescope aimpoint on the Advanced CCD Imaging Spectrometer (ACIS) S3 chip as part of a program to follow up possible X-ray detections from other facilities (PI: D. Pooley). The host galaxy, NGC 1068, has been observed many times previously with Chandra, often but not always with the High Energy Transmission Gratings in place. For a straightforward comparison to our observation, we selected the longest ACIS-S3 observation with no grating in the Chandra data archive: ObsID 344 (PI: A. Wilson), which began on 2000 February 21.7 and had an exposure time of 47.4 ks. Data reduction was performed with the chandra_repro script, part of the Chandra Interactive Analysis of Observations (CIAO) software (Fruscione et al. 2006). We used CIAO version 4.11 and calibration database version 4.8.3.

The source is clearly detected (Figure 5) with 207 total counts recorded in a 1".5 radius source extraction region in the 0.5–8 keV band. The background contribution to this X-ray

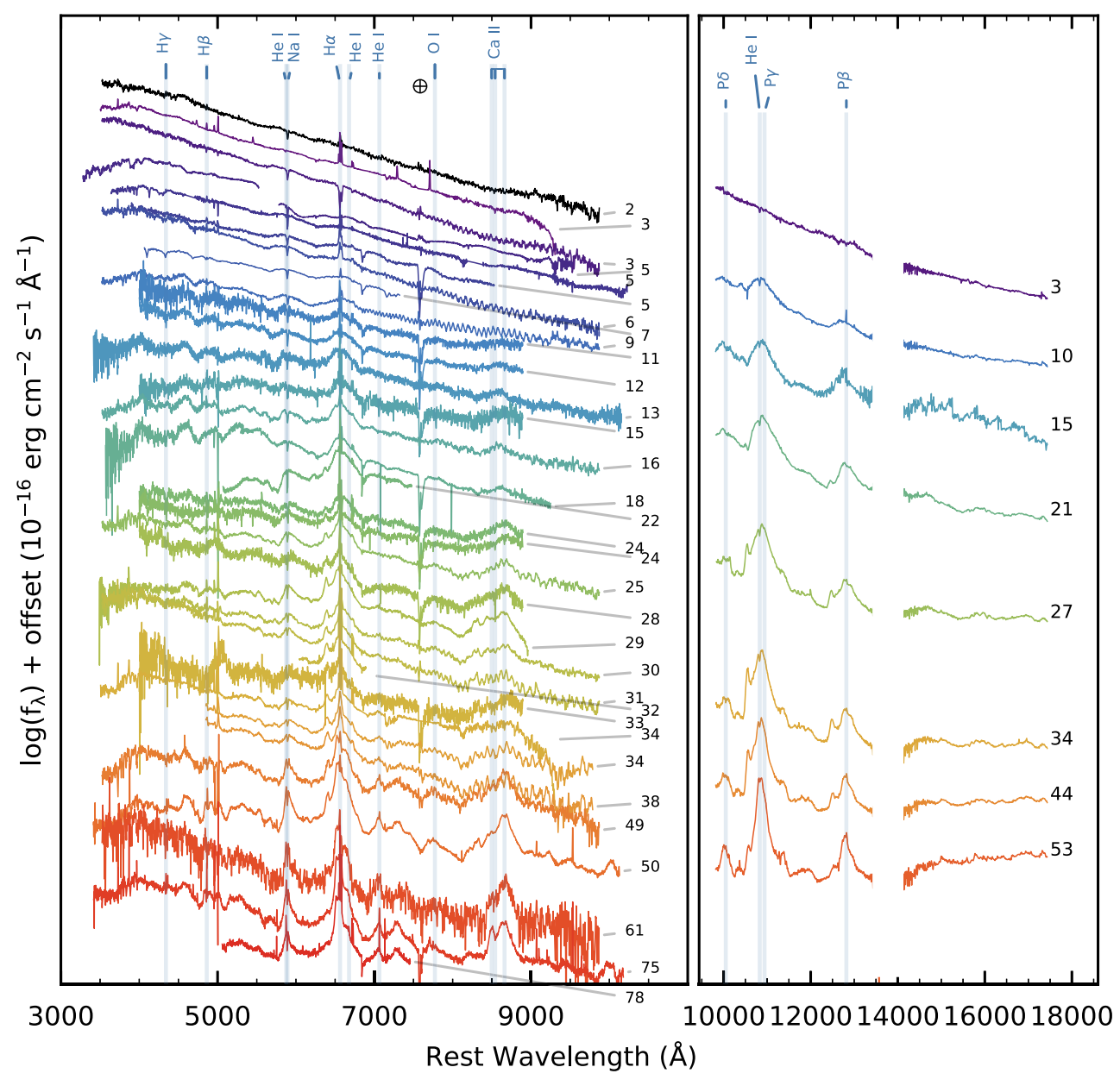


Figure 4. Left panel: the spectroscopic evolution of SN 2018ivc at optical wavelengths. SN 2018ivc shows strong emission lines and very little absorption. Imperfect background subtraction may create artificially blue continua and/or strong narrow lines in the broad $H\alpha$ emission. The phase of each spectrum is given on the right. High-resolution observations are resampled with SpectRes (Carnall 2017) to 2 Å resolution to improve the S/N. Right panel: the NIR spectroscopic evolution with the phase of the spectrum given on the right. The strong telluric absorption between 13450 and 14000 Å is masked in all NIR spectra. At the top of each panel, prominent lines are identified, and in the left panel, a prominent telluric feature is marked with a cross.

flux is nonnegligible but difficult to estimate given the nonspatially uniform X-ray emission immediately surrounding the location of SN 2018ivc in its host galaxy. One estimate of the background comes from an annular background region of inner radius $2^{\prime\prime}$ and outer radius $4^{\prime\prime}$ centered on the SN. Based on the 80 counts in this background region, there are 192 ± 14 net counts from SN 2018ivc in the 0.5–8 keV band.

To assess the spectral properties of the SN and determine its X-ray flux, we extract and simultaneously fit source and background spectra in the 0.5–8 keV band using Sherpa (Freeman et al. 2001) with the modified Cash (1979) statistic cstat and the simplex optimization method. Our model components in all cases are absorbed hot plasmas (APEC

model). We use the Tuebingen–Boulder Interstellar Medium absorption model (Wilms et al. 2000) with a minimum column density equal to the Galactic value of $n_{\rm H} = 1.55 \times 10^{19} \, {\rm cm^{-2}}$. We separately use two options for the background spectrum: the first is the annulus mentioned above in ObsID 20306, and the second is a 1.75 radius circle (identical to the source extraction region) in ObsID 344.

The first choice of background spectrum (annular extraction region from ObsID 20306) is well fit by two hot plasmas (temperatures of $kT_1 = 0.01 \, \mathrm{keV}$ and $kT_2 = 0.85 \, \mathrm{keV}$) absorbed by a column of density $3.2 \times 10^{20} \, \mathrm{cm}^{-2}$. The second choice of background spectrum (circular extraction region from ObsID 344) is also well fit by two hot plasmas (temperatures of

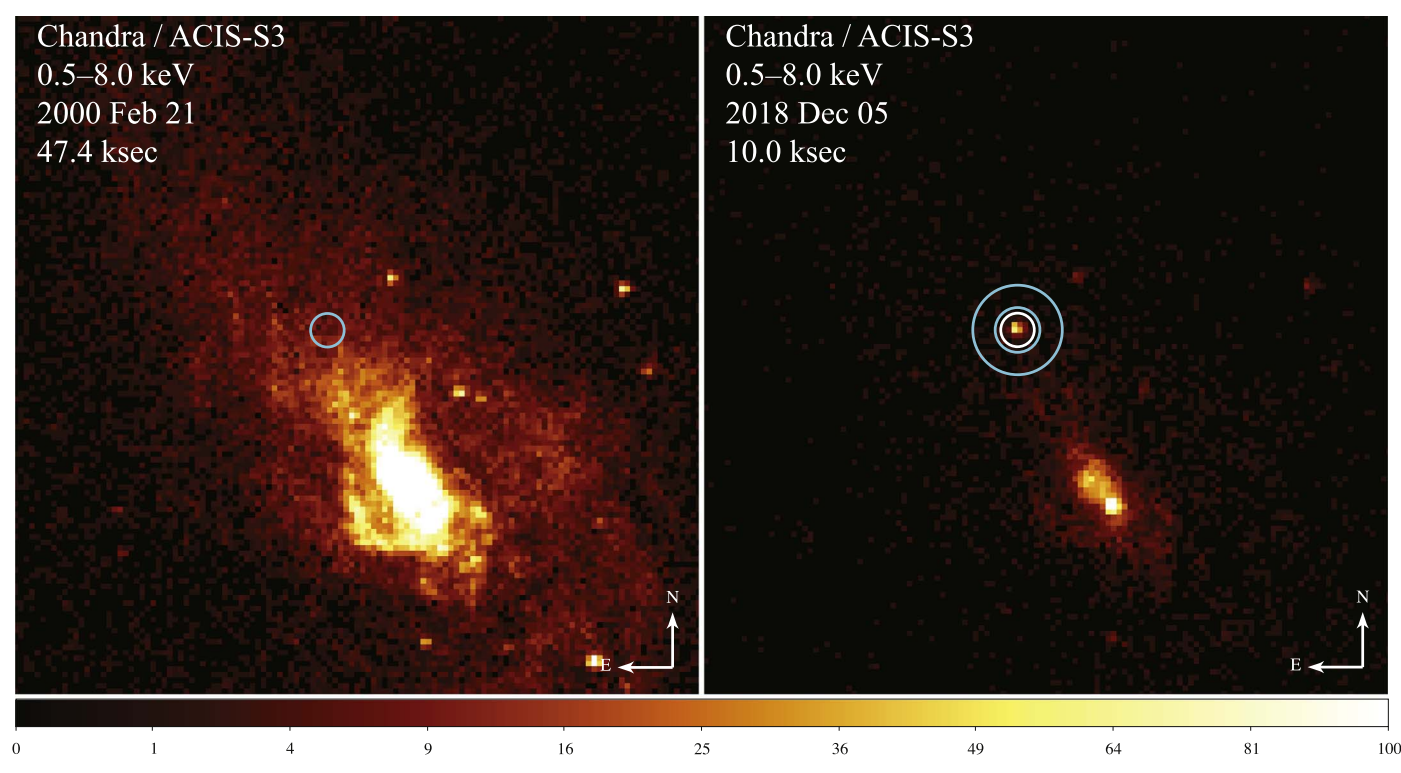


Figure 5. Pre-SN (left panel) and post-SN (right panel) images of NGC 1068 taken with Chandra/ACIS-S3. Each image is 1' on a side. The white circle in the right panel is 1."5 in radius centered on SN 2018ivc and is used to extract the source spectrum. Note the nonuniform extended emission surrounding the SN. The cyan circle in the left panel (identical to the source region) and the cyan annulus in the right panel were each used to extract background spectra. See the text for details.

 $kT_1 = 0.21 \text{ keV}$ and $kT_2 = 0.95 \text{ keV}$) absorbed by a column of density $1.6 \times 10^{19} \text{ cm}^{-2}$. Using each of these background spectra separately, we fit the SN spectrum with an absorbed plasma.

With the first choice of background, we obtain a good fit (reduced cstat of 0.63) with best-fit parameters for the SN of $n_{\rm H}=(4.4^{+0.7}_{-0.9})\times 10^{22}~{\rm cm}^{-2}$ and $kT=17^{+63}_{-7}~{\rm keV}$, with the upper limit representing the model maximum. All uncertainties are 68% confidence intervals. The intrinsic X-ray flux of the SN in this model is $(8.2\pm0.8)\times 10^{-13}~{\rm erg~cm}^{-2}~{\rm s}^{-1}$. For a distance of $10.1~{\rm Mpc}$, this corresponds to a luminosity of $L_{\rm x}=(1.0\pm0.1)\times 10^{40}~{\rm erg~s}^{-1}$.

With the second choice of background, we also obtain a good fit (reduced cstat of 0.59) with best-fit parameters for the SN of $n_{\rm H}=(3.6^{+0.8}_{-0.6})\times 10^{22}~{\rm cm^{-2}}$ and $kT=43^{+37}_{-31}$ keV with the upper limit representing the model maximum. The intrinsic X-ray flux of the SN in this model is $(7.5\pm0.7)\times 10^{-13}~{\rm erg~cm^{-2}~s^{-1}}$. For a distance of 10.1 Mpc, this corresponds to a luminosity of $L_{\rm x}=(9.2\pm0.9)\times 10^{39}~{\rm erg~s^{-1}}$.

Although the different choices for background extraction give slightly different results, they are consistent with each other within the uncertainties. In each case, the reported fluxes are integrated from the unabsorbed models. Uncertainties on those fluxes are calculated as the 68%-confidence bounds of the integrated, unabsorbed fluxes from Monte Carlo realizations (1000 samples) of the best-fit models, taking into account the uncertainties in the best-fit parameters (using the sample flux command in Sherpa)

4. Properties of the Supernova and Its Host Galaxy

4.1. Supernova Parameters

The DLT40 survey identified SN 2018ivc on 2018 November 24.07, 4.96 days after the last observation of the field on 2018

November 19.11. After the DLT40 team's prompt reporting of the SN to TNS, the Asteroid Terrestrial-impact Last Alert System (ATLAS) identified a more recent non-detection in their data on 2018 November 20.42 with a limiting magnitude of 18.6 mag in the orange-ATLAS filter. As an explosion epoch, we adopt 2018 November 22.25 \pm 1.8, the midpoint of the last non-detection (by ATLAS) and the first detection (by DLT40).

We adopt Milky Way extinction values of E(B - V) = 0.0289 ± 0.0004 mag from Schlafly & Finkbeiner (2011). Unfortunately, SN 2018ivc exploded in a region of high extinction within NGC 1068, which prevented us from deriving the extinction in the host galaxy from the Na I D lines (Poznanski et al. 2012). Instead, we estimate an extinction of $E(B-V) = 0.5 \pm 0.15$ mag by matching the color evolution of SN 2018ivc over the first 20 days with that of other SNe II (SN 1980K: Barbon et al. 1982; Buta 1982; Tsvetkov 1983; SN 1998S: Fassia et al. 2000; Liu et al. 2000; Pozzo et al. 2004; Li et al. 2011; SN 1996al: Benetti et al. 2016; SN 2012A: Tomasella et al. 2013, SN 2013by: Valenti et al. 2015, SN 2013ej: Valenti et al. 2014). While the light curves of these SNe have varying slopes, the colors are consistent during the first 20 days, which is why we choose this period to constrain the extinction. A conservative error of 0.15 mag is adopted to take into account the large uncertainty of the method. This is consistent with the extinction derived in the next section from spectroscopy of the parent H II region, and we adopt it as the host-galaxy extinction for our analysis. Throughout this paper, unless otherwise noted, we use the extinction law of Cardelli et al. (1989) with $R_V = 3.1$.

In SNe IIP/IIL, the amount of 56 Ni synthesized in the explosion can be calculated from the luminosity of the SN after the fall from the plateau ($\sim 80-100$ days post explosion), when the light curve is powered by the radioactive decay of

 $^{56}\text{Ni} \rightarrow ^{56}\text{Co} \rightarrow ^{56}\text{Fe}$. We measure the pseudo-bolometric luminosity of SN 2018ivc from the HST observations on day 220.9 by first transforming the F555W filter and the F814W filter to the Landolt V and I filters, respectively, using the relations of Harris (2018). This first step is necessary, as SN 1987A was not observed in the WFC3 F555W and F814W filters. Following Valenti et al. (2008), we find the pseudo-bolometric luminosity by integrating the apparent magnitude at the effective wavelength of each filter, using Simpson's rule. We calculate the pseudobolometric luminosity for SN 1987A from the V and I filters in the same way. Then, following Spiro et al. (2014), we calculate the nickel mass as $M(^{56}\text{Ni}) = 0.075 \, M_{\odot} \times L_{18 \text{ivc}}(t) / L_{87 \text{A}}(t)$. We find $M(^{56}\text{Ni}) = 0.0056^{+0.0036}_{-0.0022} M_{\odot}$. Uncertainties in the nickel mass were calculated using a Monte Carlo simulation taking into account normal uncertainties in the explosion epoch, distance modulus, Galactic extinction, host-galaxy extinction, and apparent magnitude of SN 2018ivc and SN 1987A. We caution that to calculate this value, we assumed that (1) there was complete γ -ray trapping, (2) we could convert HST filter magnitudes to Landolt filter magnitudes using relations derived from stellar spectral energy distributions (SEDs), and (3) SN 1987A and SN 2018ivc have the same SED. The uncertainties associated with each of these assumptions are not included in the reported uncertainties.

4.2. Host Properties

We searched in the ESO Science Portal⁴¹ for MUSE integral field unit (IFU) observations of SN 2018ivc's host galaxy, NGC 1068. It was observed on 2014 December 14 under program 094.B-0298(A), in four pointings that we combined for a total exposure time of 1180 s. All observations were reduced with the standard MUSE pipeline (Weilbacher et al. 2014) using default parameters through reflex (Freudling et al. 2013).

For each spaxel, we performed a similar analysis to that of Galbany et al. (2014, 2016a, 2016c). Briefly, using a modified version of STARLIGHT (Cid Fernandes et al. 2005; R. López Fernández et al. 2016, private communication), we model the stellar component of the continuum by estimating the fractional contribution of simple stellar populations (SSP) from the Bruzual (2007) base, adding dust attenuation effects as a foreground screen with a Fitzpatrick (1999) reddening law and $R_V = 3.1$. Our basis set is composed of 66 SSPs with 17 ages, ranging from 1 Myr to 18 Gyr, and four different metallicities (0.2, 0.4, 1.0, and 2.5 Z_{\odot}).

By subtracting the best SSP fit from each observed spectrum, we obtained a pure gas emission spectrum for each spaxel. From the pure gas spectrum, we estimated the flux of the most prominent emission lines after correcting for dust content with a correction derived from the Balmer decrement (assuming case B recombination; Osterbrock & Ferland 2006, the same extinction law, and $R_V=3.1$). From the pure gas models for each spaxel, we create an extinction-corrected ${\rm H}\alpha$ map.

We use our extinction-corrected $H\alpha$ map to identify the H II region containing SN 2018ivc (its "parent" region) and derive environmental and progenitor properties. Following Galbany et al. (2016a, 2018), the $H\alpha$ maps are used to select star-forming H II regions across the galaxy with a modified version of HIIEXPLORER⁴² (Sánchez et al. 2012), a package that detects clumps of higher intensity in a map by aggregating adjacent pixels. This procedure selected 1801 H II clumps with an

average radius of 140 pc. Once the H II regions were identified, the same analysis described above was performed on the extracted spectra. The observed spectrum and the best-fit STARLIGHT spectrum of the H II region containing SN 2018ivc can be seen in the bottom left panel of Figure 6. From this analysis and using the Cardelli et al. (1989) extinction law, we find $E(B-V)=0.37\pm0.04$ mag for the parent region of SN 2018ivc, consistent with the value derived in the previous section.

We use oxygen abundance as a proxy for metallicity, as oxygen is produced at the beginning of the enrichment process by massive stars and, by mass, comprises 50% of the heavy elements in the universe (López-Sánchez et al. 2012). Using the pure gas emission spectrum of the H II region, we determine metallicity from the O3N2 empirical calibrator (Pettini & Pagel 2004). This same spectrum is used to find the equivalent width of H α (EWH α). The upper left panel of Figure 6 shows the EWH α values for each H II region in NGC 1068. We find the metallicity to be 12 + log₁₀(O/H) = 8.6 ± 0.26, and the EWH α = 38.58 ± 0.26 Å. These host properties will be put in the context of other SNe in Section 7.

5. Supernova Evolution

The detailed evolution of SN 2018ivc was caught in the almost-daily photometric and spectroscopic observations. These revealed a rapidly evolving SN with a steeply declining light curve and spectra with broad emission.

5.1. Light-curve Evolution

The light curve of SN 2018ivc rose rapidly, peaking around day 3, only 5 days after the last non-detection. It then showed a rapid, linear decline typical of Type IIL—like SNe. Figure 7 displays a comparison of SN 2018ivc and other well-studied SNe with a variety of slopes. While the global trend is linear with a similar decline rate to SNe 1979C and 1980K, our high-cadence observations quickly revealed that there are, in the first 50 days, several changes in the slope rarely seen in other Type IIL—like SNe. SN 2018ivc is also relatively faint compared to other SNe with similar slopes.

The light curve of SN 2018ivc changes slope approximately every 10 days over the first 30 days. We fit a continuous piecewise linear function to the r-band observations, leaving the slopes, initial intercept, and breakpoints as free parameters (eight free parameters). This fit is shown in Figure 2. The initial decline ending at day 7.57 ± 0.41 has a slope of $0.1068 \pm$ 0.0094 mag day⁻¹. This is followed by a plateau until day 18.07 ± 0.45 with a slope of 0.0056 ± 0.0031 mag day⁻¹. The light curve begins to decline steeply on day 18.07, with a slope of 0.0811 ± 0.0077 mag day⁻¹. After day 27.55 ± 1.37 , the slope changes again to $0.0355 \pm 0.0014 \,\mathrm{mag \, day}^{-1}$. At no point is the slope of SN 2018ivc consistent with the slope expected for cobalt decay (0.008 mag day $^{-1}$ in R). Searching among other SNe IIP/IIL, we were only able to find one light curve in the literature that resembled the evolution (although \sim 1 mag brighter): that of SN 1996al (see Section 6.1).

We searched the DLT40 difference images in the months leading up to SN 2018ivc for a pre-explosion outburst similar to SN 2009ip ($M_r \approx -14.5$ mag; Foley et al. 2011; Mauerhan et al. 2013; Pastorello et al. 2013; Margutti et al. 2014). However, these observations do not reveal any hint of a pre-outburst eruption, with ~ 90 images of the field take in the

⁴¹ http://archive.eso.org/scienceportal/home

⁴² http://www.caha.es/sanchez/HII_explorer/

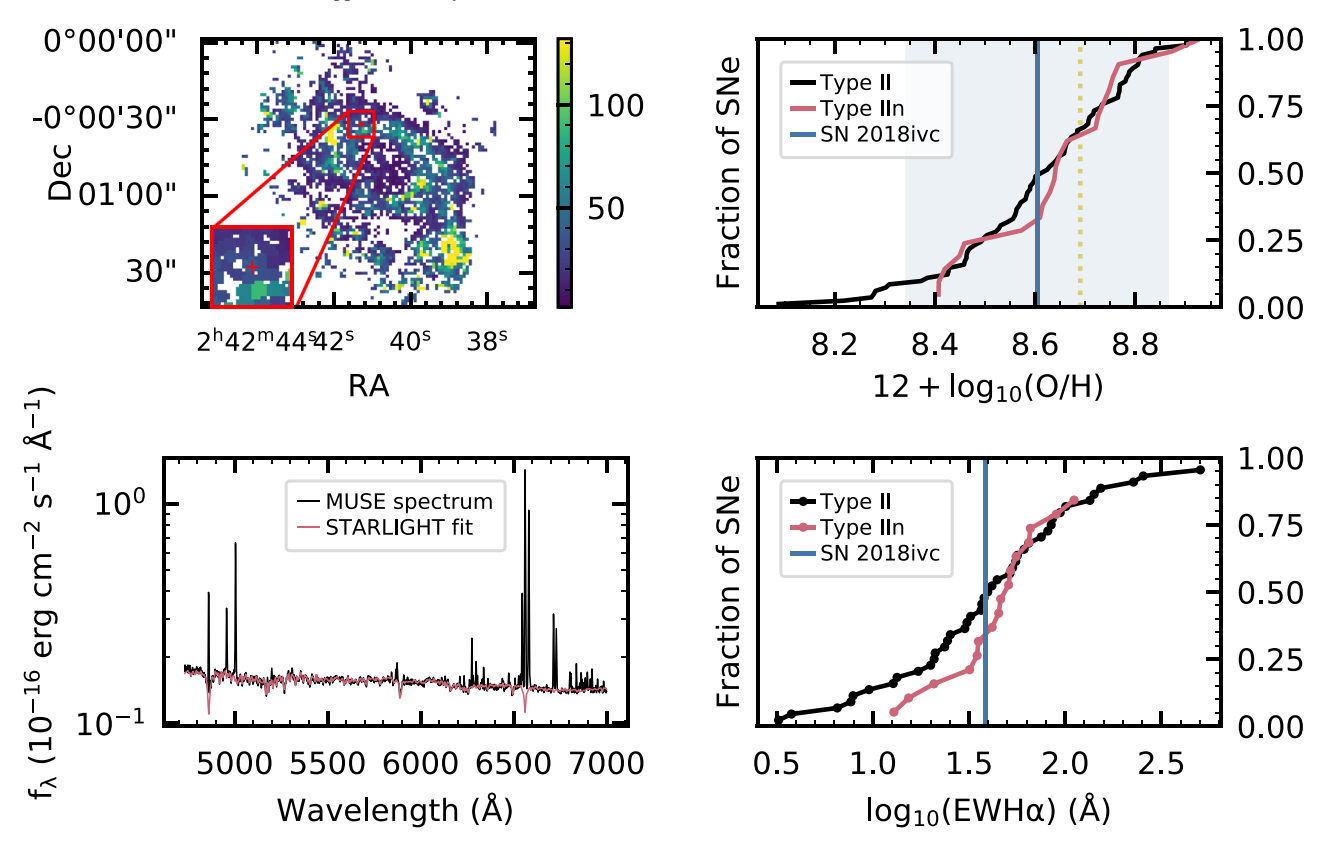


Figure 6. Upper left panel: the map of the H II regions in NGC 1068 identified by HIIEXPLORER; the parent H II region of SN 2018ivc is marked with a red point. The map is colored by $H\alpha$ equivalent width (EWH α), which is a proxy for regions with young stellar populations. A close-up view of a 10" region around the SN is shown in the inset. Lower left panel: the MUSE spectrum of the parent H II region of SN 2018ivc (black) and the STARLIGHT fit to the spectrum in pink. Upper right panel: the cumulative fraction of SNe from the PISCO sample (Galbany et al. 2018) as a function of metallicity for SNe IIP/IIL (black) and SNe IIn (pink). The metallicity of the parent H II region of SN 2018ivc is marked with a blue vertical line, and the uncertainty in this value is denoted with the light blue shaded region. Solar metallicity (8.69; Asplund et al. 2009) is plotted as a dotted yellow line. Lower right panel: the cumulative fraction of SNe as a function of EWH α of their parent H II region. The fraction of SNe IIP/IIL is shown in black, the fraction of SNe III in pink, and the EWH α of SN 2018ivc is marked with the blue vertical line.

 \sim 150 days prior to the SN explosion, with a typical limiting magnitude of $r \approx 19.3$ ($M_r \approx -12$ mag).

5.2. Spectroscopic Evolution

The spectroscopic evolution of SN 2018ivc shows strong H and He I emission and very shallow (if any) absorption. The full evolution can be seen in Figure 4, where prominent spectroscopic features are labeled.

The optical and NIR spectra obtained at 2.04 and 2.95 days, respectively, show a featureless blue continuum. By day 5, broad $H\alpha$ and HeI $\lambda5876$ emission begin to develop with similar profiles. While the presence of $H\beta$ in absorption cannot be completely ruled out (because of possible contamination from other lines), an absorption component is clearly missing from both $H\alpha$ and HeI $\lambda5876$. This is typical of SNe IIn and some Type IIL–like SNe (Gutiérrez et al. 2014). Although the physical mechanism for the lack of absorption is still unclear, possible explanations include a low-density (possibly low-mass) envelope and scattering off of CSM (Schlegel 1996).

The Ca II $\lambda\lambda$ 8498, 8542, 8662 emission triplet begins to develop at day 12 and strengthens through day 78. On day 30, the He I λ 7065 line begins to show in emission. By day 75, the He I λ 6678 line is visible in the red wing of the H α emission; this feature may be blended in earlier spectra. The shape of the emission around H α in the two spectra from days 75 and 78 is very boxy, which we will discuss more in later sections. We

obtained a low signal-to-noise ratio (S/N) spectrum at day 279 that shows a broad H α profile, similar to that seen on day 78.

The NIR spectra are dominated by hydrogen and He I emission features. The blue continuum at day 3 gives way to Paschen emission features by day 10. The He I $\lambda 10830$ line is blended in the P γ feature. In both the optical and the NIR, the widths of the emission lines decrease with time as the speed of the ejecta decreases.

The spectra of SN 2018ivc show potential narrow emission lines on top of the broad $H\alpha$ emission. This region is heavily contaminated by the host-galaxy emission, which is challenging to separate from the $H\alpha$ SN emission in all but the highest-resolution observations. We searched for an SN component in our highest-resolution spectrum: the MMT/Binospec observation from 2018 December 14. In this spectrum, we fit a Gaussian profile to night-sky lines, galaxy emission lines, and $H\alpha$. We find the FWHM intensity of the narrow $H\alpha$ emission (\sim 130 km s⁻¹) to be consistent with that of the other galaxy emission lines ([N II] $\lambda\lambda$ 6548, 6583; [S II] $\lambda\lambda$ 6716, 6731).

We measure the velocity evolution using the half-width at half-maximum (HWHM) intensity of Gaussian fits to the H α , He I λ 5876, and P β emission lines and the minimum of the Fe II and H β absorption features. The velocities are shown in Figure 8, with velocities measured from emission features in the left panel and velocities measured from absorption features

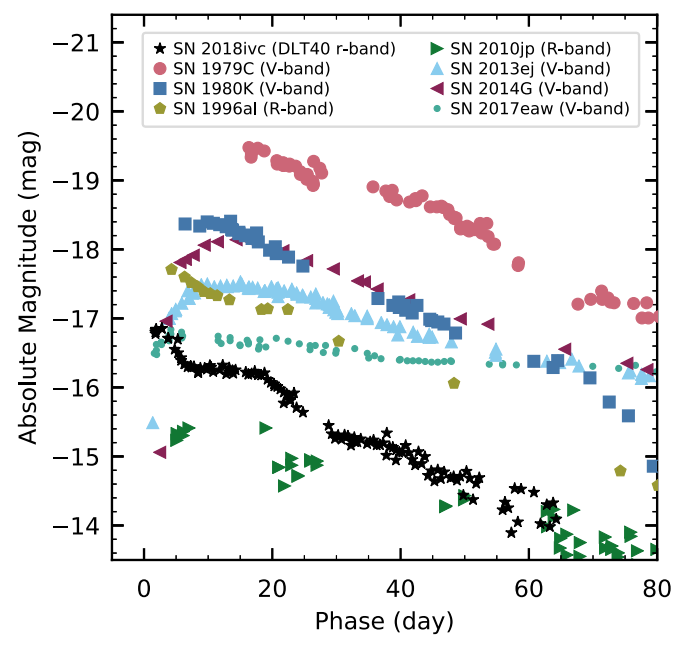


Figure 7. Light curve of SN 2018ivc (black stars; DLT40 *r* band) compared to a sample of well-studied SNe. SNe with a variety of slopes are represented with an emphasis on Type IIL—like SNe. The best-observed filter is shown for each SN. SN 1979C (pink circles, *V* band; Balinskaia et al. 1980; de Vaucouleurs et al. 1981; Barbon et al. 1982) and SN 1980K (blue squares, *V* band; Barbon et al. 1982; Buta 1982; Tsvetkov 1983) represent the historical Type IIL—like class. SN 2017eaw (sea foam green points, *V* band; Szalai et al. 2019) represents the Type IIP—like SNe. SN 2013ej (light blue triangles, *V* band; Valenti et al. 2014) and SN 2014G (maroon arrows, *V* band; Terreran et al. 2016) are transitional Type IIL—like objects, with a clear fall from the plateau onto the radioactive decay tail. We plot two SNe that will be discussed later in the text in comparison to SN 2018ivc: SN 2010jp (green arrows, *R* band; Smith et al. 2012) and SN 1996al (yellow pentagons, *R* band; Benetti et al. 2016).

in the right panel. We note that while there is asymmetry, substructure, and host contamination in individual features, the trends are consistent across features, giving us confidence in the overall velocity evolution. However, we caution that there may be significant scatter in individual measurements. The H α velocity can be compared to the average of 112 SNe IIP/IIL, calculated by Gutiérrez et al. (2017). We find that the velocities are similar to those found in SNe IIP/IIL and higher than the velocities of SN 1996al. However, the evolution is more rapid, with the initial velocity higher than average and the final velocities lower than average. The Fe II lines are also broadly consistent with the average Type IIP/IIL evolution, although there is considerable scatter. We simultaneously fit Fe II $\lambda\lambda 4924$, 5018, but we were unable to simultaneously fit Fe II $\lambda\lambda$ 4924, 5018, 5169 and, therefore, fit Fe II λ 5169 separately. Velocities from both fits are shown in Figure 8.

On day 18, emission features begin to develop in the blue wing of the emission-line profiles of $H\alpha$, $H\beta$, He I λ 5876, Ca II triplet, He I λ 10830, and P β (see the first five panels of Figure 9). These features gain strength until day \approx 35, after which they fade until they are barely visible on day 78. We identify the emission lines that appear blueward of the rest wavelengths of these features as a high-velocity (HV) component owing to its presence at the same velocity in each feature (see the right panel of Figure 9). From the blueshifted peak of the emission, we find the velocity of the emitting

material to be $\sim 9000 \, \mathrm{km \ s^{-1}}$ at day 18, slowing down to $\sim 7000 \, \mathrm{km \ s^{-1}}$ by day 78.

6. Analysis

6.1. Comparison to 1996al

Figure 10 (left panel) shows the r-band light curve of SN 2018ivc in black compared with the R-band light curve of SN 1996al in pink, shifted by 1.0 mag. Since there are no stringent detection limits to constrain the explosion epoch for SN 1996al, we use an explosion epoch of 1996 July 19, which is 18 days later than the reference epoch suggested by Benetti et al. (2016). They compare the light curve to that of other Type IIL-like SNe and estimate 1996 July 1 as the V-band maximum, which they adopt as the reference epoch. However, given the similarity between SN 1996al and SN 2018ivc, using the latter to constrain the explosion of SN 1996al may be more appropriate. While SN 2018ivc is very well sampled, the sparse sampling of SN 1996al, especially after the initial decline, makes a detailed comparison challenging. Nevertheless, the light curve of SN 1996al does show a relatively steep decline, at a similar rate as SN 2018ivc, which, like SN 2018ivc, is interrupted by a short plateau.

A spectroscopic comparison of SN 1996al (gray) and SN 2018ivc (color) is shown in the right panel of Figure 10. As described above, the phases are with respect to a reference time of 1996 July 19 for SN 1996al. There is broad agreement in the spectral evolution of both SNe, with H and He I emission lines dominating the spectra and little to no absorption. The widths of the emission features of SN 1996al are smaller than those of SN 2018ivc, implying a higher ejecta velocity for SN 2018ivc. This is quantified in the left panel of Figure 8, which shows that the velocity of H α is slower in SN 1996al than in SN 2018ivc and that the H α velocity declines more rapidly than that of SN 1996al.

Given the overall similarity between SN 2018ivc and SN 1996al, here, we will summarize the main results of Benetti et al. (2016) for SN 1996al and compare these two objects more closely. SN 1996al was identified as a transition SN between a Type IIL-like and Type IIn with a linearly declining light curve and a week-long plateau starting around day 15. The spectra show broad hydrogen and He I emission with narrow P Cygni lines superimposed. From ground-based preexplosion $H\alpha$ images, a $25 M_{\odot}$ luminous blue variable progenitor was identified. Light-curve modeling of the 15 yr evolution showed that the light curve is dominated by ejecta-CSM interaction. The linear decline of the light curve, the velocity evolution, and the evolution of the H α flux a year after explosion indicated a low ejecta mass and that the ejecta were predominantly composed of helium. Benetti et al. (2016) interpret the similarity in the shapes of the hydrogen and helium emission-line profiles as evidence that both of these lines originate in the interaction region during at least the first 50 days of evolution. The low velocities and multicomponent emission lines point to a dense, asymmetric CSM, while the narrow P Cygni lines indicate a patchy, symmetric CSM at a larger radius. The asymmetric CSM is confirmed in a multicomponent $H\alpha$ profile in a nebular spectrum from day 142.

Given the peculiarity of the light curve and spectroscopic evolution of SN 2018ivc, the qualitative similarity to SN 1996al during the first 80 days of evolution (before it

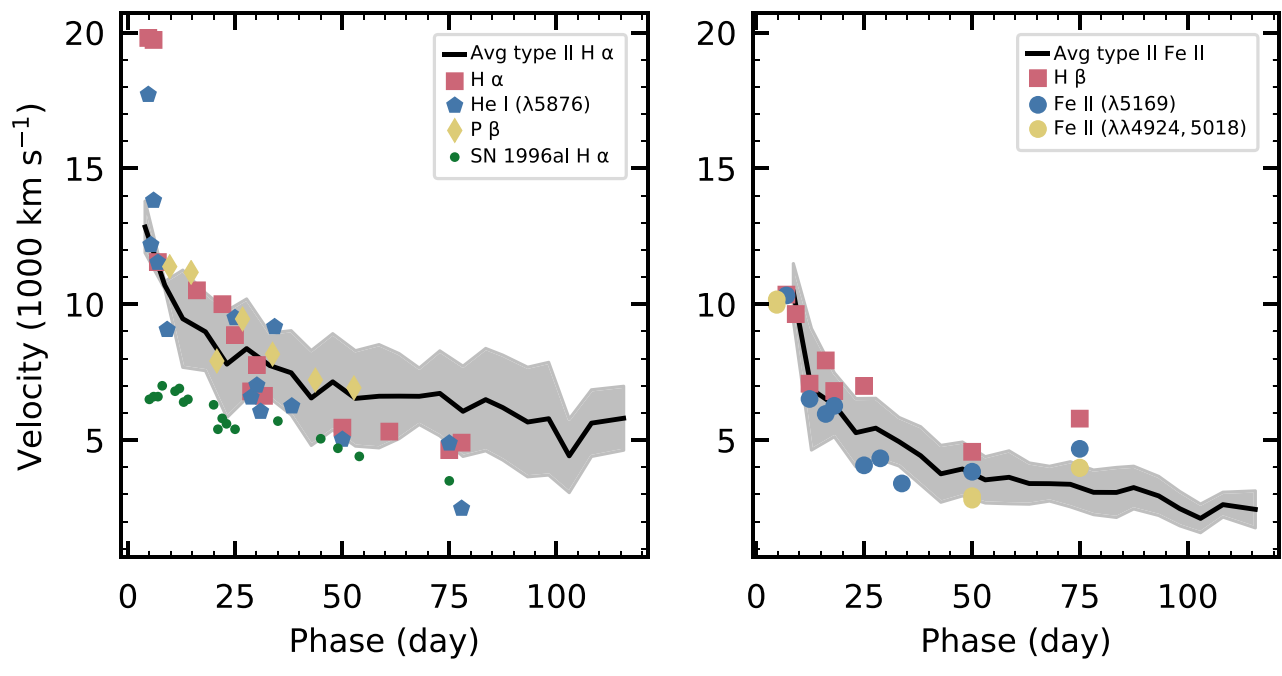


Figure 8. Left panel: the expansion velocity evolution of SN 2018ivc found using the HWHM of emission lines H α (pink squares), He I (blue pentagons), and P β (yellow diamonds). The H α velocity of SN 1996al is shown by green circles. The velocity of SN 2018ivc is similar to that of other SNe IIP/IIL, although it evolves more rapidly than most, including SN 1996al. Right panel: the expansion velocity evolution of SN 2018ivc found using the minimum wavelength of the absorption features H β (pink squares) and Fe II (blue and yellow circles). The average H α velocity (left panel) and Fe II (right panel) of the Gutiérrez et al. (2017) sample of SNe IIP/IIL is shown in black with the standard deviation in gray.

disappeared behind the Sun) is striking. The light curves decline at similar rates and show similar changes in slope, including a short plateau. Additionally, their spectra are dominated by emission lines from the same species. The steeply declining light curve and short plateau of SN 2018ivc could be a sign of a low mass of hydrogen in its ejecta. Benetti et al. (2016) model the light curve of SN 1996al and find that the light from the ejecta is significantly fainter than the light from the CSM. The fact that SN 2018ivc is less luminous than SN 1996al indicates that the majority of the light may be coming from the SN ejecta, although the frequent changes in slope demonstrate that the CSM-ejecta interaction is significant at some phases.

Additionally, the similarity of the hydrogen and He I emission profiles indicates that they originate in the same part of the ejecta and that perhaps, like SN 1996al, the ejecta of SN 2018ivc are predominantly helium. While multi-peaked emission profiles are not observed in the early-time spectra of SN 2018ivc, asymmetry is seen spectroscopically in the HV feature that appears around day 18. The broad H α profile in the day 279 spectrum of SN 2018ivc does not show multiple components. It is possible that the SN 2018ivc has a multicomponent H α profile, like the one clearly visible in SN 1996al, but that the two components are blended to the point of being indistinguishable from a single profile. Given the similarity between SN 2018ivc and SN 1996al, it is possible that they have similar progenitors, as we will discuss in Section 7.

6.2. Progenitor from HST Pre-imaging

High-resolution images taken prior to explosion can be used to identify and characterize the properties of an SN progenitor (e.g., Smartt et al. 2004; Maund & Smartt 2005, 2009; Li et al. 2007; Mattila et al. 2008; Smartt 2009; Elias-Rosa et al. 2010, 2011;

Fraser et al. 2010, 2011, 2014; Crockett et al. 2011; Kochanek et al. 2012, 2017; Maund et al. 2013, 2014; Tomasella et al. 2013; van Dyk 2017; Kilpatrick & Foley 2018; van Dyk et al. 2019). We located pre-explosion HST observations in the Mikulski Archive for Space Telescopes (MAST) and analyzed them for the presence of a progenitor. The SN site is located in the Advanced Camera for Surveys/Wide Field Channel (ACS/WFC) data in bands F658N and F814W from program GO-9788 (PI: L. Ho) and in F550M from GO-9503 (PI: N. Nagar), as well as Wide Field Planetary Camera (WFPC2) images in F606W from both GO-5479 (PI: M. Malkan) and GO-8597 (PI: M. Regan) and in F450W from GO-11128 (PI: D. Fisher); see Table 2.

To precisely pinpoint the SN location in the archival data, we subsequently obtained higher spatial resolution HST images of the SN with the WFC3 on 2019 July 1. We identify 69 sources in common between between the F814W WFC3 image of the SN and the GO-9788 F814W ACS exposure, and we use these to identify the SN location in the pre-explosion ACS image. To do this, we randomly select 34 sources and use these to compute the astrometric transformation from the WFC3 image to the ACS image with the PyRAF task geomap. We then measure the location of the SN in the pre-explosion image using the PyRAF task geoxytran and the astrometric transformation from geomap. To understand the error introduced by the sources used to find the astrometric transformation, we calculate the rms uncertainty of the 35 stars not used to determine the transformation. We repeat this process 1000 times and find the SN to be located at pixel $(3546.990 \pm 0.011 \pm 0.062, 4069.583 \pm 0.008 \pm 0.049)$ in the ACS F814W image, where the first uncertainty reported is the standard deviation of the measured SN location over the 1000 trials, and the second uncertainty corresponds to the median rms uncertainty of the stars not used to calculate the

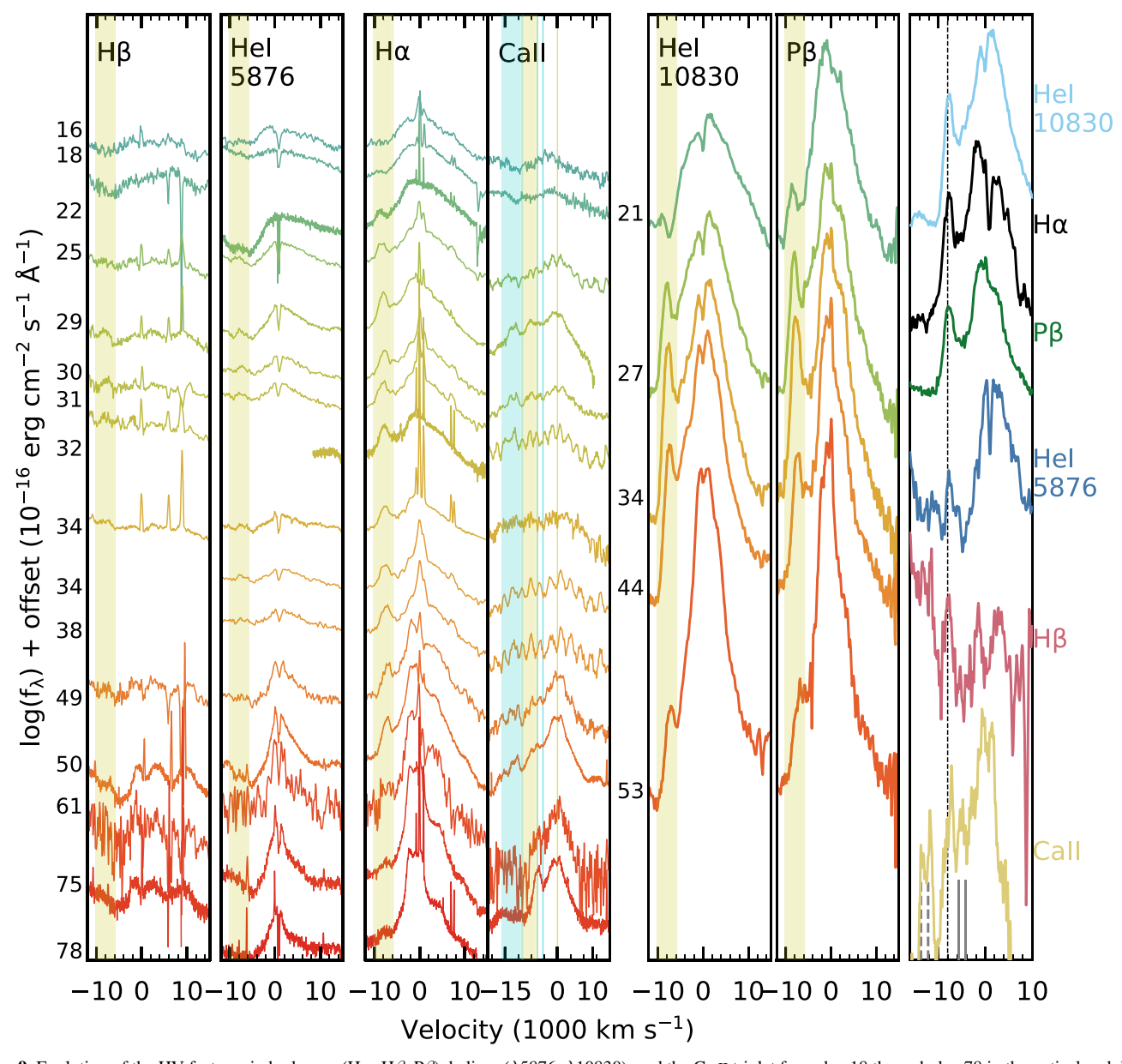


Figure 9. Evolution of the HV features in hydrogen ($\text{H}\alpha$, $\text{H}\beta$, $\text{P}\beta$), helium ($\lambda 5876$, $\lambda 10830$), and the Ca II triplet from day 18 through day 78 in the optical and day 21 through day 53 in the NIR. The feature is most prominent in $\text{H}\alpha$, $\text{P}\beta$, and $\text{He I}\lambda 10830$. The panels are labeled in the upper left corner with the feature they present. The yellow shaded region marks -10,000 to -6000 km s⁻¹. The phases of the optical spectra are marked to the left of the first panel, and the NIR phases are marked to the left of the He I $\lambda 10830$ panel. The Ca II panel is centered on the $\lambda 8662$ component of the triplet (marked in yellow at both rest wavelengths and shaded in yellow at HV). The two blue components are marked at rest wavelength with vertical cyan lines and at high velocity with a shaded cyan region. The last panel shows the optical features on day 30 and the NIR features on day 34 for all emission lines in which the HV feature is seen. The HV feature is marked with a dashed line at -8000 km s⁻¹, and each emission feature is labeled to the right of the panel. The bluest two Ca II triplet features that are offset in velocity space are marked with a solid line gray at the velocity corresponding to their rest wavelengths and with a dashed gray line for the HV features.

astrometric transformation. No source is detected within 5σ of this location, as indicated in Figure 11.

We then processed the individual archival FLC and C0F frames through AstroDrizzle (Hack et al. 2012) to flag cosmic-ray hits and then extracted photometry from these frames using Dolphot (Dolphin 2000, 2016). Given that the progenitor is not detected in the pre-explosion HST images, we place upper limits on the progenitor detection, which we list in Table 2.

We note in passing that, owing to the relative proximity of SN 2018ivc to the active nucleus of NGC 1068, the various pre-explosion data of the host galaxy obtained by the Spitzer Space Telescope, even at the shortest-wavelength IRAC band

at 3.6 μ m, are of little value for progenitor identification, since the image of the nucleus was too luminous and effectively saturated the detectors. Given the comparatively low Spitzer spatial resolution, the pixels at the SN site were heavily affected by this saturation.

7. Discussion

The immediate identification and high-cadence photometric and spectroscopic follow-up observations offer us a detailed picture of the evolution of SN 2018ive that would not otherwise be possible. Although the declining light curve indicates that this is a Type IIL—like SN, there is evidence that the progenitor is

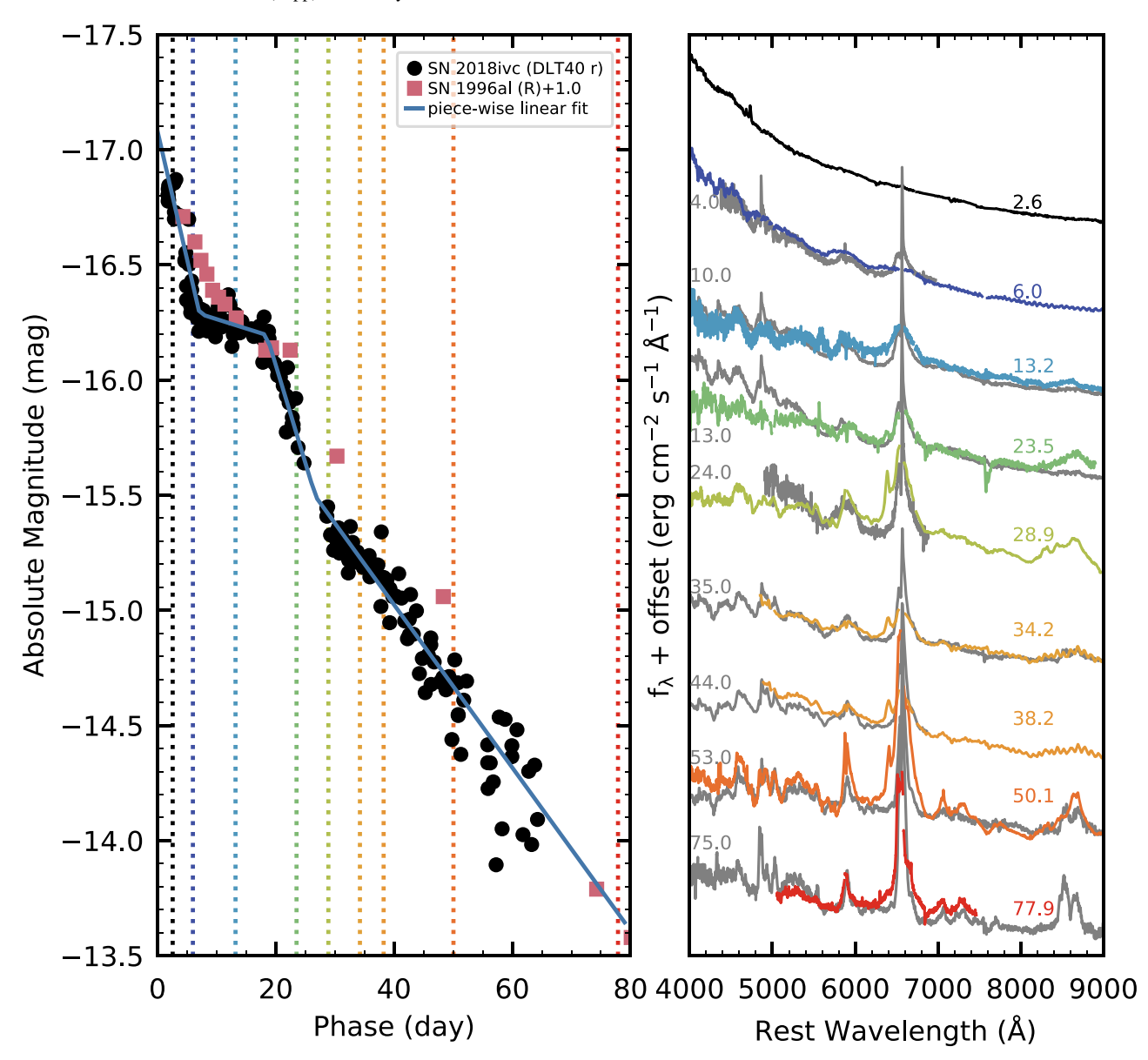
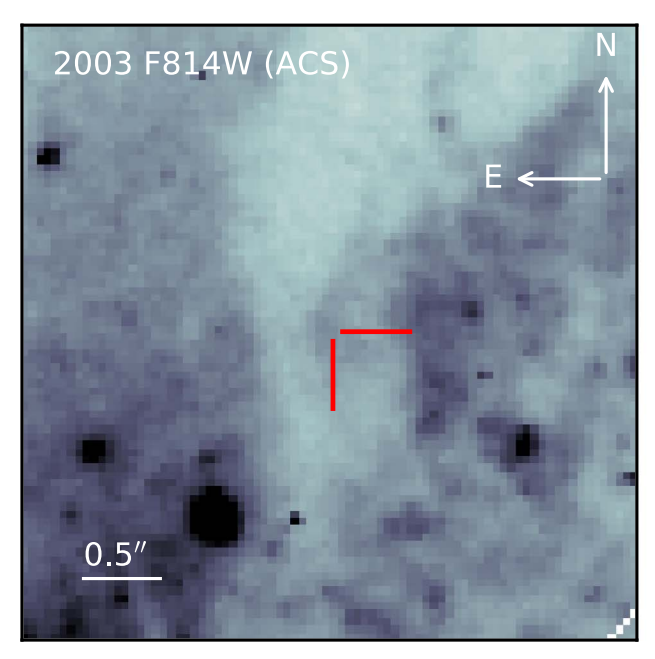


Figure 10. Comparison of the photometric and spectroscopic evolution of SN 2018ivc to the similar event SN 1996al. Left panel: the *r*-band light curve of SN 2018ivc (black) compared with the *R*-band light curve of SN 1996al (pink). The light curve of SN 1996al has been shifted down by 1.0 mag to align with the SN 2018ivc light curve, and the explosion epoch is set to 1996 July 19. The piecewise linear fit of the SN 2018ivc light curve is shown in blue. The dashed vertical lines correspond to the phase of the spectra plotted on the right. Right panel: the spectroscopic evolution of SN 2018ivc (colored spectra) compared with that of SN 1996al (gray spectra). The phases of SN 2018ivc are given on the right side of the panel in color and the phases of SN 1996al are given on the left side of the panel in gray. The spectra of SN 1996al have been offset to align with those of SN 2018ivc. Although SN 1996al does not show the HV features and SN 2018ivc does not have narrow lines (the host contamination visible in Figure 4 has been masked out of the spectra of SN 2018ivc), SN 2018ivc and SN 1996al are spectroscopically similar with strong He I and hydrogen features in emission.

more complicated than that of the typical Type IIL—like SN. The strong He I lines, not always visible in Type IIL—like SNe, could indicate that the progenitor lost most of its hydrogen envelope. The rapidly declining light curve corroborates this picture of mass loss. The frequent change in slope suggests that, in addition to the linear decay of the small hydrogen envelope, the shock is encountering shells of different densities that were ejected from the star during its lifetime. This would imply that some interaction between the SN and the CSM is also partially powering the light curve of SN 2018ivc, even though narrow lines typical of some interacting SNe (IIn) are not detected.

The narrow lines ($\sim 10^2$ km s⁻¹) of SNe IIn are formed by the recombination of unshocked CSM that has been ionized by

photons from the forward-shock front. CSM can also produce intermediate-width lines ($\sim 10^3~\rm km~s^{-1}$) from the recombination of gas after the shock wave has passed through it. In SN 2018ivc, we observe broad emission from the SN ejecta and narrow emission from the host galaxy but find no evidence that a narrow line SN component exists (see Section 5.2). This lack of narrow lines may indicate a clumpy CSM that has been enveloped by the SN ejecta (Smith et al. 2015; Andrews & Smith 2018). We note, however, that SNe IIn do not always exhibit narrow lines at all epochs, and it is possible that we do not have a high-resolution observation during the time that narrow lines were visible. Additionally, it is possible that the narrow lines from the CSM are not strong enough to show above broad lines of the ejecta or



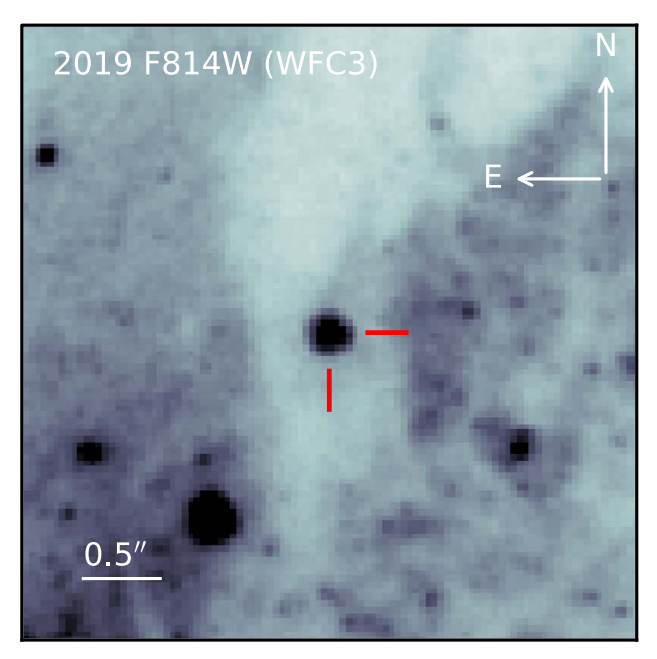


Figure 11. Left panel: pre-explosion HST ACS/WFC image from 2003 October 26 at F814W of NGC 1068 containing the site of SN 2018ivc. No source is identified at the SN location, indicated by the red ticks. Right panel: HST WFC3/UVIS image at F814W of SN 2018ivc, obtained on 2019 July 1. The SN is indicated with the red ticks.

Table 2
HST Upper Limits to the SN 2018ivc Progenitor Detection

Data	T.,	E:14	A M	All-4- M	D ID	DI
Date	Instrument	Filter	Apparent Mag Limit (3σ)	Absolute Mag Limit (3σ)	Program ID	PI
2007 Aug 16	WFPC2	F450W	>25.8	>-6.2	GO-11128	D. Fisher
2003 Jan 8	ACS/WFC	F550M	>25.0	>-6.5	GO-9503	N. Nagar
1994 Dec 3	WFPC2	F606W	>25.0	>-6.4	GO-5479	M. Malkan
2001 Jun 30	WFPC2	F606W	>25.4	>-6.0	GO-8597	M. Regan
2003 Oct 26	ACS/WFC	F658N	>23.4	>-7.9	GO-9788	L. Ho
2003 Oct 26	ACS/WFC	F814W	>24.4	>-6.5	GO-9788	L. Ho

are too narrow and weak to be distinguished from the significant host contamination.

Despite the lack of narrow lines, there are several other indications that the ejecta of SN 2018ivc are interacting with CSM. The boxy profiles of the H α and He I λ 6678 complex could also be indicative of interaction with a shell of CSM (Andrews et al. 2010; Inserra et al. 2011). The strong X-ray detection likely originates from the shocked CSM. Together, the light curve and spectroscopic observations demonstrate the presence of interaction in SN 2018ivc.

The HV features seen in SN 2018ivc are unusual. The presence of these features indicates that hot, dense, asymmetric material is moving with the speed of the ejecta (if the material is in the line of sight) or faster. Given that the HV features are present in hydrogen, helium, and calcium emission, this feature may be due to material that was ejected in the explosion. It is possible that a bullet of ⁵⁶Ni was ejected early in the explosion at high speed and that its the radioactive decay powers these features.

Searching the literature, we find that while multicomponent hydrogen features are seen in SNe IIP/IIL, they are most often during the nebular phase and at a significantly lower velocity. Two notable exceptions to this are SN 2014G (Terreran et al. 2016) and SN 2010jp (Smith et al. 2012). SN 2014G was a Type IIL–like SN that showed narrow flash spectroscopic

features during the first 10 days of evolution. Around day 100, SN 2014G developed a narrow feature blueward of $H\alpha$ that could not be associated with any other species and, thus, was identified as an HV hydrogen feature, with an initial velocity of \sim 7600 km s⁻¹. Terreran et al. (2016) explained this feature as being caused by the spherically symmetric SN ejecta interacting with a bipolar lobe CSM with a 40° angle between the CSM axis and the observer's line of sight. SN 2010jp was a low-luminosity, linearly declining SN IIn that showed a triple-peaked $H\alpha$ emission line. The red and blue $H\alpha$ peaks (-12,000 and 15,000 km s⁻¹, respectively) are explained by a jet-powered explosion. The HV features in SN 2018ivc, at comparable speeds to those of SN 2014G and SN 2010jp, could originate from a disk or jet-like structure.

Based on the upper limits we derive from the HST preexplosion images (see Table 2 and Figure 12) and the fact that hydrogen is visible and strong throughout the spectroscopic evolution, we evaluate what we can infer about the progenitor. Referring to the single-star evolutionary tracks at solar metallicity from the MESA Isochrones & Stellar Tracks (MIST v1.2; Choi et al. 2016; Dotter 2016; Paxton et al. 2011, 2013, 2015), we exclude stars whose photometry would exceed our upper limits or with less than $0.1\,M_\odot$ of hydrogen in the envelope. With these criteria, we find that we can eliminate all stars with initial masses between $9\,M_\odot$ and $48\,M_\odot$ and above

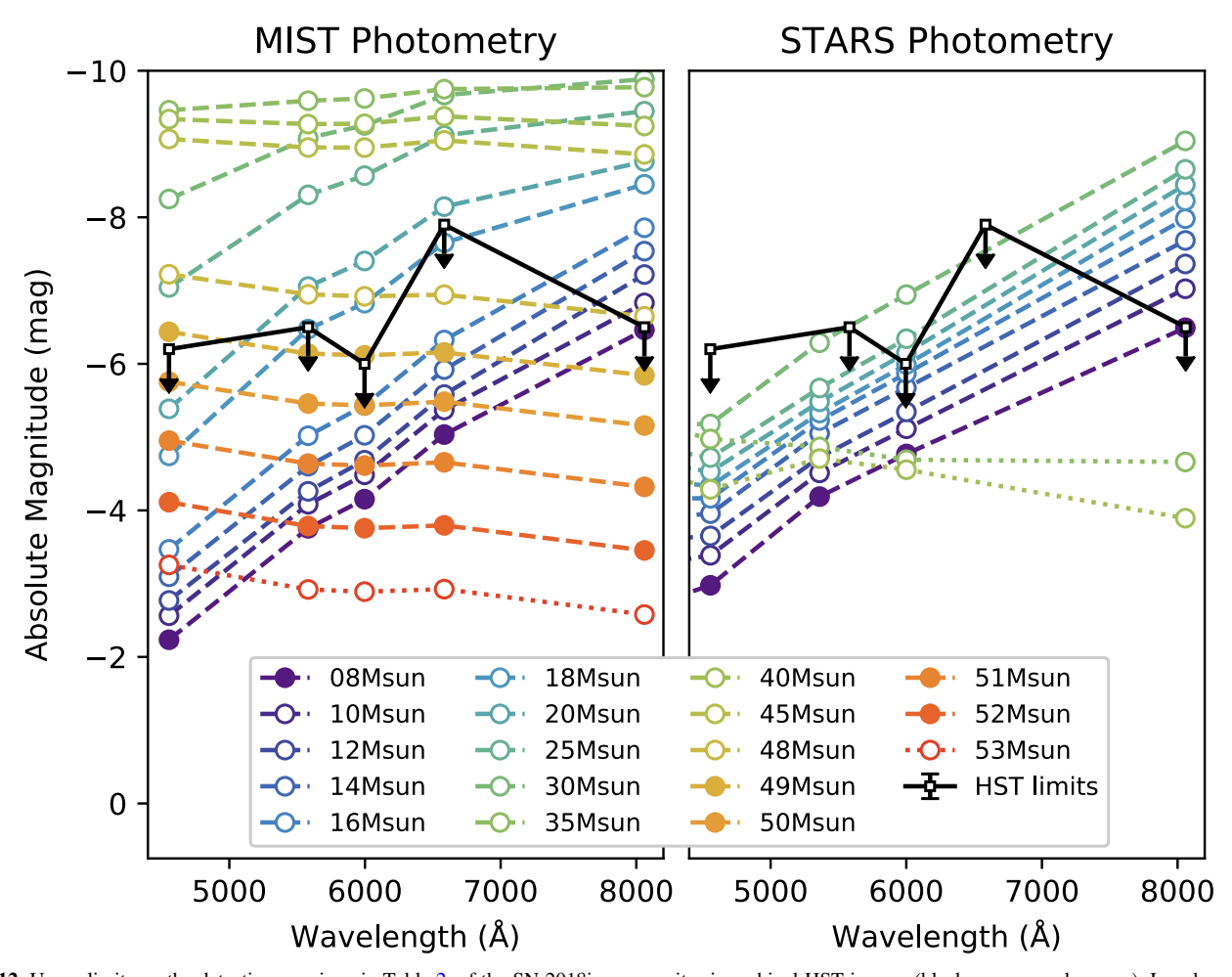


Figure 12. Upper limits on the detection, as given in Table 2, of the SN 2018ivc progenitor in archival HST images (black squares and arrows). In color are model SEDs derived from the endpoint of the solar-metallicity MIST (Choi et al. 2016; Dotter 2016; Paxton et al. 2011, 2013, 2015) single-star evolutionary tracks (left panel) and the STARS models (right panel; Eggleton 1971; Pols et al. 1995; Eldridge & Tout 2004) for masses spanning the range of allowed masses for each evolutionary model code. Allowed models are denoted with filled color circles. Models that are ruled out by the upper limits are marked with open circles and connected by a dashed line. Models that are ruled out by a lack of hydrogen in their envelope ($M_{\rm H,env} < 0.1~M_{\odot}$) are denoted with open circles and connected by a dotted line. The HST upper limits and strong hydrogen features in the spectra imply that that progenitor of SN 2018ivc, if single, was likely 8 M_{\odot} . The MIST models allow for additional progenitors in the range 49–52 M_{\odot} ; although, these have small hydrogen envelopes that may not be able to produce the features seen in the spectra of SN 2018ivc.

 $52\,M_\odot$ as the progenitor (see the left panel of Figure 12). We conservatively include stars between $49\,M_\odot$ and $52\,M_\odot$; although, we note that the largest hydrogen envelope mass in this range is $0.5\,M_\odot$, which could possibly be excluded with detailed spectroscopic modeling that is beyond the scope of this paper. Additionally, we caution that this limit is highly dependent on the evolutionary models used. For instance, if we adopt the STARS models (Eggleton 1971; Pols et al. 1995; Eldridge & Tout 2004; on which the BPASS binary evolution models are based, e.g., Eldridge et al. 2017), we find that the hydrogen mass in the envelope drops below $0.1\,M_\odot$ at a lower mass and redder SED, resulting in the exclusion of all stars with masses greater than $8\,M_\odot$ (see the right panel of Figure 12).

The majority of massive stars form in binary systems (Sana et al. 2012). For this reason, we also consider possible binary progenitor systems by examining the endpoints of the BPASS v2.2 models and the light from each combined system. Again, considering the HST upper limits and the mass of hydrogen in the envelope, we find a maximum progenitor mass of $11\,M_\odot$, with the majority of progenitors between $8\,M_\odot$ and $9\,M_\odot$ (see Figure 13). Most progenitor systems are in a wide binary with

log(Period [day]) = 2.75 for masses between $8\,M_\odot$ and $11\,M_\odot$ and a broader range of log(Period) (2.5–4) for an $8\,M_\odot$ progenitor. The few short-period progenitors occur when the secondary mass is much smaller than the primary mass $(M_2/M_1\leqslant 0.2)$; see Figure 14).

To better understand the nature of SN 2018ivc and its progenitor, we compare the host properties derived in Section 4.2 with those of all SNe IIP/IIL (85) and SNe IIn (16) from the PMAS/PPak Integral-field Supernova hosts COmpilation (PISCO) sample (Galbany et al. 2018). The metallicity of the parent H II region of SN 2018ivc is near the median of the SN IIP/IIL distribution and slightly below the median of the SN IIn distribution (see the upper right panel of Figure 6). Similarly, the EWH α falls near the median of both SN IIP/IIL and SN IIn distributions.

 $EWH\alpha$ is an indicator of the age of the cluster. Kuncarayakti et al. (2013) show a theoretical relationship between $EWH\alpha$ and the age of the stellar population assuming a Salpeter initial mass function (IMF) and an instantaneous burst of star

⁴³ Updated with all new observations obtained through 2019 May.

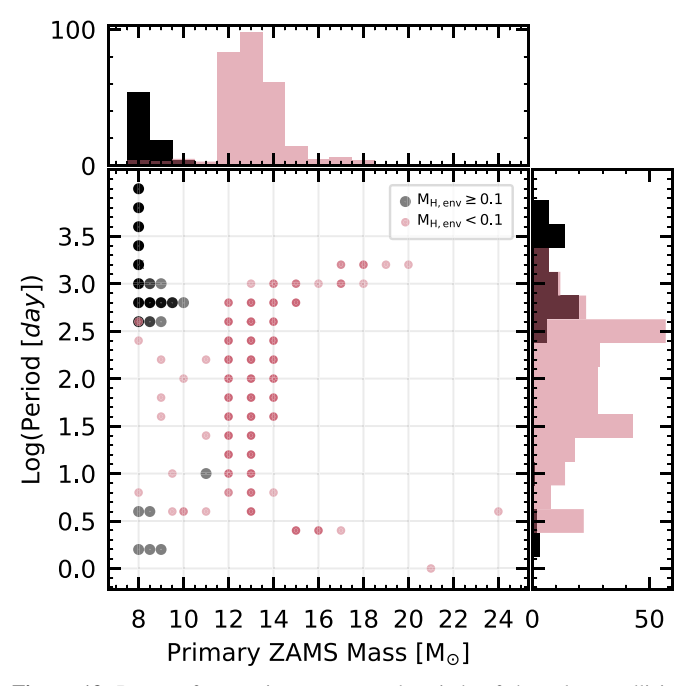


Figure 13. Range of progenitor masses and periods of the solar-metallicity model binary systems from BPASS (Eldridge et al. 2017) that are allowed by the pre-explosion upper limits. Models that also contain more than $0.1~M_{\odot}$ of hydrogen in their envelopes are marked as black circles, while models that contain less hydrogen are marked as pink points. The model parameters are marginalized over the ratio of the secondary to primary star mass (see Figure 14 for an animation of the three-dimensional distribution). The opacity of the markers indicates the density of models at a given location. The distribution of progenitor masses, further marginalized over the period, is shown in the top panel, with allowed progenitors in black and eliminated progenitors in pink. Similarly, the distribution of periods, further marginalized over progenitor mass, is shown in the bottom right panel with the same color scheme. Consistent with the single stars, we find that the progenitor was less than $12~M_{\odot}$ and most probably $8~M_{\odot}$.

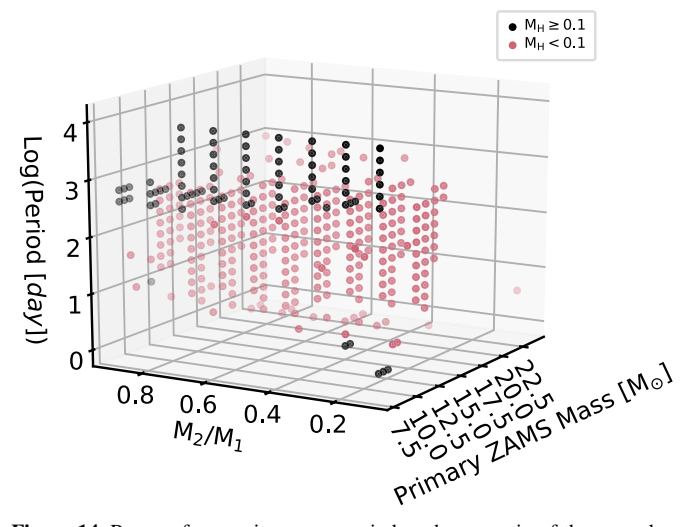


Figure 14. Range of progenitor mass, period, and mass ratio of the secondary to the primary star of the solar-metallicity model binary systems from BPASS (Eldridge et al. 2017) that are allowed by the pre-explosion upper limits. Models that are allowed by both the HST upper limits and the hydrogen in their envelopes are shown in black, and models that are ruled out are shown in pink. Most mass ratios are possible for allowed log(Period [days]) and progenitor masses; although, there are six models that only occur at specific combinations of all three parameters.

(An animation of this figure is available.)

formation. The age of the stellar population can then be used to estimate the age of the SN progenitor. Using the EWH α derived from the parent HII region and Figure 1 from Kuncarayakti et al. (2013), we find the age of the progenitor of SN 2018ive to be 6.75–7.75 Myr (depending on the slope and upper value of the IMF), corresponding to a progenitor mass of 25–28 M_{\odot} . This value is similar to the 25 M_{\odot} of SN 1996al found by Benetti et al. (2016). We note, however, that this agreement may be coincidental owing to limitations in our ability to isolate a single stellar population at this distance as well as simplifying assumptions made in mapping of the EWH α modeling to progenitor age (see Schady et al. 2019 for a detailed explanation). Specifically, the EWH α -age relation used assumes that (1) massive stars are the ionizing source producing the $H\alpha$ emission, (2) we recover all of the photons ionizing the surrounding gas (i.e., there is no leakage), and (3) there are no binaries in the stellar population. The inclusion of these effects could yield an older age and, therefore, a lowermass progenitor, which is more consistent with the constraints from pre-explosion imaging.

8. Summary

In this paper, we have described the early discovery and prompt follow-up observations of SN 2018ivc by the DLT40 team and high-cadence monitoring by the GSP over the first 80 days of evolution. The DLT40 survey observed SN 2018ivc, identified it as an SN candidate using automated software, and confirmed the SN with follow-up observations within 15 minutes of the discovery observation. This discovery triggered a comprehensive set of photometric and spectroscopic observations by the DLT40 team and the GSP for the duration of visibility, \sim 80 days.

The light curve of this SN changed slope every $\sim \! 10$ days for the first 30 days before settling onto a linear decline. The spectroscopic evolution is rapid, and the spectrum is dominated by H and He I emission lines with shallow or no P Cygni absorption. These characteristics combined with the X-ray detection suggest that the SN ejecta are interacting with CSM. We find HV emission in hydrogen, helium, and calcium, indicating an asymmetric progenitor or explosion. We analyze the pre-explosion IFU observations of NGC 1068 and find that SN 2018ivc exploded in a region of typical metallicity and star formation with respect to other SNe II. By analyzing the EWH α of the SN's parent H II region, we find evidence that the progenitor of SN 2018ivc had an initial mass of $\leqslant \! 25\,M_{\odot}$.

We show that SN 2018ivc resembles SN 1996al both photometrically and spectroscopically, indicating that the progenitor of SN 2018ivc may have been similar to the $25\,M_\odot$ progenitor inferred for SN 1996al; although, this is in tension with the progenitors derived from pre-explosion observations. Finally, we use HST archival observations of NGC 1068, taken prior to explosion, and ToO HST observations of the SN to derive photometric upper limits on the progenitor. From these limits and the strong presence of hydrogen in the spectra, we infer a probable low-mass progenitor ($M < 12\,M_\odot$ for binary models and $M < 8\,M_\odot$ for single-star models; although, the MIST models do allow for a massive progenitor ($49 \le M \le 52\,M_\odot$).

It is only with the early discovery, immediate response, and high-cadence monitoring of SNe, like those provided by the DLT40 and GSP teams, that the complex and rapid evolution of interacting SNe like SN 2018ivc can be observed and characterized. It is possible that the interaction in other Type IIL—like SNe, lacking narrow lines and without early identification and sufficient follow-up observations, has not been identified. For a clear and detailed understanding of the progenitor systems of SNe II, specifically, the role of mass loss in stellar evolution and its observational signatures, we must continue to identify SNe early, announce the discovery immediately, and combine our resources for high-cadence observations of the full SN evolution.

We are grateful to B. J. Fulton for providing us the image shown in Figure 1, to P. Chandra for analysis of the Swift XRT and GMRT data, and to Jared Goldberg, Charlie Kilpatrick, Morgan Fraser, and Stephen Smartt for insightful conversations. We are grateful to the referee for the insightful comments. Research by K.A.B., S.V., and Y.D. is supported by NSF grant AST-1813176. Research by D.J.S. is supported by NSF grants AST-1821967, 1821987, 1813708, 1813466, and 1908972. Research by J.E.A. and N.S. was supported by NSF grant AST-151559. L.G. was funded by the European Union's Horizon 2020 research and innovation programme under the Marie Skłodowska-Curie grant agreement No. 839090. J.B., D.H., C.M., and D.A.H. are supported by NSF grant AST-1313484. I.A. is a CIFAR Azrieli Global Scholar in the Gravity and the Extreme Universe Program and acknowledges support from that program, from the Israel Science Foundation (grant numbers 2108/18 and 2752/19), from the United States—Israel Binational Science Foundation (BSF), and from the Israeli Council for Higher Education Alon Fellowship. A.V.F. is grateful for financial assistance from the Christopher R. Redlich Fund, the TABASGO Foundation, and the Miller Institute for Basic Research in Science (UC Berkeley). The research of J.C.W. is supported by NSF grant AST-1813825. K.M. acknowledges the support from Department of Science and Technology (DST), Government of India and Indo-US Science and Technology Forum (IUSSTF) for the WISTEMM fellowship and the Department of Physics, UC Davis, where part of this work was carried out. P.J.B.'s work on SOUSA and core-collapse supernovae is supported by NASA ADAP grants NNX13AF35G and NNX17AF43G. D.P. gratefully acknowledges support provided by the National Aeronautics and Space Administration (NASA) through Chandra Award No. GO8-19051X issued by the Chandra X-ray Center, which is operated by the Smithsonian Astrophysical Observatory for and on behalf of NASA under contract NAS8-03060. J.Z. is supported by the National Natural Science Foundation of China (NSFC, grants 11773067 and 11403096), the Youth Innovation Promotion Association of the CAS (grant 2018081), and the Western Light Youth Project. The work of X.W. is supported by the National Natural Science Foundation of China (NSFC grants 11325313 and 11633002) and the National Program on Key Research and Development Project (grant 2016YFA0400803). E.B. and J.D. are supported in part by NASA grant NNX16AB25G. This work was partially supported by the Open Project Program of the Key Laboratory of Optical Astronomy, National Astronomical Observatories, Chinese Academy of Sciences.

We thank the support staffs at the many observatories where data were obtained. Funding for the Li-Jiang 2.4 m telescope

(LJT) has been provided by the Chinese Academy of Sciences and the People's Government of Yunnan Province. The LJT is jointly operated and administrated by Yunnan Observatories and Center for Astronomical Mega-Science, CAS. This work makes use of observations from the Las Cumbres Observatory network. Based in part on observations obtained at the Gemini Observatory under programs GS-2018B-Q-130 (PI: D. Sand). Gemini is operated by the Association of Universities for Research in Astronomy, Inc., under a cooperative agreement with the NSF on behalf of the Gemini partnership: the NSF (United States), the National Research Council (Canada), CONICYT (Chile), Ministerio de Ciencia, Tecnología e Innovación Productiva (Argentina), and Ministério da Ciência, Tecnologia e Inovação (Brazil). The data were processed using the Gemini IRAF package. We thank the queue service observers and technical support staff at Gemini Observatory for their assistance. This work is based in part on observations made with the NASA/ESA Hubble Space Telescope, obtained from the Data Archive at the Space Telescope Science Institute (STScI), which is operated by the Association of Universities for Research in Astronomy (AURA), Inc., under NASA contract NAS 5-26555. Support for program GO-15151 was provided by NASA through a grant from STScI. The LBT is an international collaboration among institutions in the United States, Italy, and Germany. LBT Corporation partners are The University of Arizona on behalf of the Arizona university system; Istituto Nazionale di Astrofisica, Italy; LBT Beteiligungsgesellschaft, Germany, representing the Max-Planck Society, the Astrophysical Institute Potsdam, and Heidelberg University; The Ohio State University; and The Research Corporation, on behalf of The University of Notre Dame, University of Minnesota, and University of Virginia. This research has made use of the NASA/IPAC Extragalactic Database (NED), which is operated by the Jet Propulsion Laboratory, California Institute of Technology, under contract with NASA. Observations using Steward Observatory facilities were obtained as part of the large observing programme AZTEC: Arizona Transient Exploration and Characterization. Some observations reported here were obtained at the MMT Observatory, a joint facility of the University of Arizona and the Smithsonian Institution. The LBT/MODS observations were obtained as part of a pilot effort at Steward Observatory to move to queue observing and include back-up programs for poor weather conditions or technical failures. We thank J. Power for coordinating the queue efforts for our LBT/MODS observations. Based in part on observations obtained at the Southern Astrophysical Research (SOAR) telescope, which is a joint project of the Ministério da Ciência, Tecnologia, Inovações e Comunicações (MCTIC) do Brasil, the U.S. National Optical Astronomy Observatory (NOAO), the University of North Carolina at Chapel Hill (UNC), and Michigan State University (MSU). The facilities at IAO and CREST are operated by the Indian Institute of Astrophysics, Bangalore. This research has made use of data obtained from the Chandra Data Archive and software provided by the Chandra X-ray Center (CXC) in the application packages CIAO and Sherpa. Some of the data presented herein were obtained at the W. M. Keck Observatory, which is operated as a scientific partnership among the California Institute of Technology, the University of California, and NASA; the observatory was made possible by the generous financial support of the W. M. Keck Foundation.

Facilities: ARC (DIS), ARIES:ST, ARIES:DFOT, Beijing:2.16 m (BFOSC), CTIO:PROMPT, Gemini:South (Flamingos-2), CXO, HCT (HFOSC), HET (LRS2), HST (ACS, WFPC2, WFC3), Keck: I (LRIS), Keck: II (DEIMOS), Las Cumbres Observatory (FLOYDS, Sinistro), LBT (MODS), MAST, MMT (Binospec), PO:1.2 m, SALT (RSS), SOAR (Goodman), SO: Bok (SPOL), SO: Kuiper (Mont4K) SO:SuperLOTIS, UMN:1.52 m, Spitzer (IRAC, MIPS), Swift (UVOT), YAO:2.4 m (YFOSC).

Software: astropy (Astropy Collaboratio et al. 2013; The Astropy Collaboration et al. 2018), LCOGTSNPIPE (Valenti et al. 2016), CIAO (Fruscione et al. 2006), Sherpa (Freeman et al. 2001), SpectRes (Carnall 2017).

Appendix Spectroscopic Observations

Table A1 shows a detailed log of the spectroscopic observations of SN 2018ivc.

 Table A1

 Log of Spectroscopic Observations

Observation Date	MJD	Phase	Telescope	Instrument	Wavelength Range (Å)	Exposure Time (s)	Resolution $\lambda/\Delta\lambda$
Date		(day)					
2018 Nov 24	58446.29	2.04	FTN	FLOYDS	3499–10000	2700	400–700
2018 Nov 24	58446.50	2.25	2.16 m XLO	BFOSC	3852–8696	3000	250-800
2018 Nov 24	58446.70	2.45	2.4 m LJT	YFOSC	3400–9100	1200	240
2018 Nov 24	58446.81	2.56	SALT	RSS	3494–9392	1793	600–2000
2018 Nov 25	58447.20	2.95	Gemini-S	FLAMINGOS-2	9852–18075	720	900
2018 Nov 25	58447.38	3.13	FTN	FLOYDS	3499–10000	1200	400–700
2018 Nov 25	58447.52	3.27	2.16 m XLO	BFOSC	3852–8696	3300	250–800
2018 Nov 25	58447.60	3.35	HCT-IIA	HFOSC	3500–8998	1200	1200
2018 Nov 26	58448.57	4.32	2.16 m XLO	BFOSC	3852–8697	3300	250-800
2018 Nov 27	58449.16	4.91	HET	lrs2	3640–10298	606	1140–1920
2018 Nov 27	58449.32	5.07	LBT	MODS	3290–5549	2400	1850–2300
2018 Nov 27	58449.32	5.07	LBT	MODS	5800–9572	2400	1850–2300
2018 Nov 27	58449.61	5.36	2.16 m XLO	BFOSC	3853-8701	3300	250–800
2018 Nov 28	58450.23	5.98	FTN	FLOYDS	3499–10000	1200	400–700
2018 Nov 29	58451.25	7.00	Bok	SPOL	4001–7549	2400	430
2018 Dec 01	58453.40	9.15	FTN	FLOYDS	3499-10000	1200	400–700
2018 Dec 2	58454.00	9.75	Gemini-S	FLAMINGOS-2	9851–18077	1080	900
2018 Dec 3	58455.69	11.44	HCT-IIA	HFOSC	3500–8998	1200	1200
2018 Dec 4	58456.59	12.34	HCT-IIA	HFOSC	3500–8998	1200	1200
2018 Dec 5	58457.44	13.19	Keck I	LRIS	3136–10220	119	750–1475
2018 Dec 7	58459.20	14.95	Gemini-S	FLAMINGOS-2	9849–18077	1080	900
2018 Dec 7	58459.55	15.30	HCT-IIA	HFOSC	3500-8998	1800	1200
2018 Dec 8	58460.36	16.11	FTN	FLOYDS	3500–9999	1200	400–700
2018 Dec 10	58462.32	18.07	3.5 m APO	DIS	3374–5607	2400	2450
2018 Dec 10	58462.32	18.07	3.5 m APO	DIS	5263-9404	2400	3150
2018 Dec 11	58463.81	19.56	HCT-IIA	HFOSC	3500-8998	2400	1200
2018 Dec 13	58465.00	20.75	Gemini-S	FLAMINGOS-2	9850–18077	1440	900
2018 Dec 14	58466.30	22.05	MMT	Binospec	5072–7541	720	3590
2018 Dec 15	58467.76	23.51	HCT-IIA	HFOSC	3500–8998	2400	1200
2018 Dec 16	58468.65	24.40	HCT-IIA	HFOSC	3500-8998	2400	1200
2018 Dec 17	58469.23	24.98	FTN	FLOYDS	3500–10000	1800	400–700
2018 Dec 18	58470.51	26.26	2.16 m XLO	BFOSC	4358–8690	2400	250–800
2018 Dec 19	58471.10	26.85	Gemini-S	FLAMINGOS-2	9852–18076	1800	900
2018 Dec 21	58473.15	28.90	SOAR	GHTS	3500–7000	780	1050
2018 Dec 21	58473.15	28.90	SOAR	GHTS	5000–9000	780	1050
2018 Dec 22	58474.35	30.10	FTN	FLOYDS	3499–9999	3600	400–700
2018 Dec 23	58475.21	30.96	FTN	FLOYDS	3499–9999	3600	400–700
2018 Dec 24	58476.63	32.38	HCT-IIA	HFOSC	3500–8998	2400	1200
2018 Dec 24	58476.78	32.53	HCT-IIA	HFOSC	3500–8998	1200	1200
2018 Dec 24	58476.85	32.60	SALT	RSS	6057–7010	2464	2200–5500
2018 Dec 26	58478.10	33.85	Gemini-S	FLAMINGOS-2	9849–18077	1800	900
2018 Dec 26	58478.48	34.23	FTS	FLOYDS	4800–10000	3600	400–700
2018 Dec 26	58478.83	34.58	SALT	RSS	3497–9393	2093	600–2000
2018 Dec 30	58482.49	38.24	FTS	FLOYDS	4800–9999	3600	400–700
2019 Jan 3	58486.30	42.05	FTN	FLOYDS	3500–10000	3600	400–700
2019 Jan 5	58488.00	43.75	Gemini-S	FLAMINGOS-2	9851–18075	1800	900
2019 Jan 6	58489.54	45.29	2.16 m XLO	BFOSC	3851–8692	3600	250–800
2019 Jan 10	58493.33	49.08	FTN	FLOYDS	3499–10000	3600	400–700
2019 Jan 11	58494.30	50.05	Keck I	LRIS	3137–10197	420	750–1475
2019 Jan 13	58496.49	52.24	2.16 m XLO	BFOSC	4095–8810	3000	250–800

Table A1 (Continued)

Observation Date	MJD	Phase (day)	Telescope	Instrument	Wavelength Range (Å)	Exposure Time (s)	Resolution $\lambda/\Delta\lambda$
2019 Jan 14	58497.10	52.85	Gemini-S	FLAMINGOS-2	9850-18079	2160	900
2019 Jan 22	58505.26	61.01	FTN	FLOYDS	3499-9999	3600	400-700
2019 Jan 28	58511.44	67.19	2.16 m XLO	BFOSC	3869-8822	3600	250-800
2019 Feb 5	58519.25	75.00	Keck I	LRIS	3138-10244	1200	750-1475
2019 Feb 8	58522.13	77.88	MMT	Binospec	5062-7522	960	3590
2019 Aug 28	58723.59	279.34	Keck II	DEIMOS	4480–9510	1200	1875

ORCID iDs

- K. A. Bostroem https://orcid.org/0000-0002-4924-444X
- S. Valenti https://orcid.org/0000-0001-8818-0795
- D. J. Sand https://orcid.org/0000-0003-4102-380X
- J. E. Andrews https://orcid.org/0000-0003-0123-0062
- S. D. Van Dyk https://orcid.org/0000-0001-9038-9950
- L. Galbany https://orcid.org/0000-0002-1296-6887
- D. Pooley https://orcid.org/0000-0003-4897-7833
- R. C. Amaro https://orcid.org/0000-0002-1546-9763
- N. Smith https://orcid.org/0000-0001-5510-2424
- S. Yang https://orcid.org/0000-0002-2898-6532
- G. C. Anupama https://orcid.org/0000-0003-3533-7183
- I. Arcavi https://orcid.org/0000-0001-7090-4898
- E. Baron https://orcid.org/0000-0001-5393-1608
- P. J. Brown https://orcid.org/0000-0001-6272-5507
- D. Hiramatsu https://orcid.org/0000-0002-1125-9187
- R. Dastidar https://orcid.org/0000-0001-6191-7160
- J. M. DerKacy https://orcid.org/0000-0002-7566-6080
- S. Ertel https://orcid.org/0000-0002-2314-7289
- A. V. Filippenko https://orcid.org/0000-0003-3460-0103
- O. D. Fox https://orcid.org/0000-0003-2238-1572
- G. Hosseinzadeh https://orcid.org/0000-0002-0832-2974
- D. A. Howell https://orcid.org/0000-0003-4253-656X
- A. Gangopadhyay https://orcid.org/0000-0002-3884-5637
- S. W. Jha https://orcid.org/0000-0001-8738-6011
- B. Kumar https://orcid.org/0000-0001-7225-2475
- M. Lundquist https://orcid.org/0000-0001-9589-3793
- D. Milisavljevic https://orcid.org/0000-0002-0763-3885
- C. McCully https://orcid.org/0000-0001-5807-7893
- P. Milne https://orcid.org/0000-0002-0370-157X
- K. Misra https://orcid.org/0000-0003-1637-267X
- D. E. Reichart https://orcid.org/0000-0002-5060-3673
- A. Singh https://orcid.org/0000-0003-2091-622X
- J. Vinko https://orcid.org/0000-0001-8764-7832
- X. Wang https://orcid.org/0000-0002-7334-2357
- Y. Wang https://orcid.org/0000-0002-7531-603X
- J. C. Wheeler https://orcid.org/0000-0003-1349-6538
- G. G. Williams https://orcid.org/0000-0002-3452-0560
- J. Zhang https://orcid.org/0000-0002-8296-2590

References

Anderson, J. P., González-Gaitán, S., Hamuy, M., et al. 2014, ApJ, 786, 67 Andrews, J. E., Gallagher, J. S., Clayton, G. C., et al. 2010, ApJ, 715, 541 Andrews, J. E., Sand, D. J., Valenti, S., et al. 2019, ApJ, 885, 43 Andrews, J. E., & Smith, N. 2018, MNRAS, 477, 74 Arcavi, I., Gal-Yam, A., Cenko, S. B., et al. 2012, ApJL, 756, L30 Asplund, M., Grevesse, N., Sauval, A. J., & Scott, P. 2009, ARA&A, 47, 481 Astropy Collaboratio, Robitaille, T. P., Tollerud, E. J., et al. 2013, A&A, 558, A33

Balinskaia, I. S., Bychkov, K. V., & Neizvestnyi, S. I. 1980, A&A, 85, L19 Barbon, R., Ciatti, F., & Rosino, L. 1979, A&A, 72, 287

Barbon, R., Ciatti, F., Rosino, L., Ortolani, S., & Rafanelli, P. 1982, A&A,

Benetti, S., Chugai, N. N., Utrobin, V. P., et al. 2016, MNRAS, 456, 3296 Blinnikov, S. I., & Bartunov, O. S. 1993, A&A, 273, 106

Breeveld, A. A., Curran, P. A., Hoversten, E. A., et al. 2010, MNRAS, 406, 1687

Brown, P. J., Breeveld, A. A., Holland, S., Kuin, P., & Pritchard, T. 2014, Ap&SS, 354, 89

Brown, T. M., Baliber, N., Bianco, F. B., et al. 2013, PASP, 125, 1031

Bruzual, G. 2007, in ASP Conf. Ser. 374, From Stars to Galaxies: Building the Pieces to Build Up the Universe, ed. A. Vallenari et al. (San Francisco, CA:

Buta, R. J. 1982, PASP, 94, 578

Cardelli, J. A., Clayton, G. C., & Mathis, J. S. 1989, ApJ, 345, 245

Carnall, A. C. 2017, arXiv:1705.05165

Cash, W. 1979, ApJ, 228, 939

Choi, J., Dotter, A., Conroy, C., et al. 2016, ApJ, 823, 102

Cid Fernandes, R., Mateus, A., Sodré, L., Stasińska, G., & Gomes, J. M. 2005, S, 358, 363

Crockett, R. M., Smartt, S. J., Pastorello, A., et al. 2011, MNRAS, 410, 2767 de Vaucouleurs, G., de Vaucouleurs, A., Buta, R., Ables, H. D., & Hewitt, A. V. 1981, PASP, 93, 36

Dolphin, A. 2016, DOLPHOT: Stellar Photometry v2.0, Astrophysics Source Code Library, ascl:1608.013

Dolphin, A. E. 2000, PASP, 112, 1383

Dotter, A. 2016, ApJS, 222, 8

Eggleton, P. P. 1971, MNRAS, 151, 351

Eldridge, J. J., Stanway, E. R., Xiao, L., et al. 2017, PASA, 34, e058

Eldridge, J. J., & Tout, C. A. 2004, MNRAS, 353, 87

Elias-Rosa, N., van Dyk, S. D., Li, W., et al. 2010, ApJL, 714, L254

Elias-Rosa, N., van Dyk, S. D., Li, W., et al. 2011, ApJ, 742, 6

Faran, T., Poznanski, D., Filippenko, A. V., et al. 2014a, MNRAS, 442, 844 Faran, T., Poznanski, D., Filippenko, A. V., et al. 2014b, MNRAS, 445, 554

Fassia, A., Meikle, W. P. S., Vacca, W. D., et al. 2000, MNRAS, 318, 1093

Filippenko, A. V. 1982, PASP, 94, 715

Filippenko, A. V. 1997, ARA&A, 35, 309

Fitzpatrick, E. L. 1999, PASP, 111, 63

Foley, R. J., Berger, E., Fox, O., et al. 2011, ApJ, 732, 32

Fraser, M., Ergon, M., Eldridge, J. J., et al. 2011, MNRAS, 417, 1417

Fraser, M., Maund, J. R., Smartt, S. J., et al. 2014, MNRAS, 439, L56

Fraser, M., Takáts, K., Pastorello, A., et al. 2010, ApJL, 714, L280

Freeman, P., Doe, S., & Siemiginowska, A. 2001, Proc. SPIE, 4477, 76

Freudling, W., Romaniello, M., Bramich, D. M., et al. 2013, A&A, 559, A96 Fruscione, A., McDowell, J. C., Allen, G. E., et al. 2006, Proc. SPIE, 6270, 62701V

Galbany, L., Anderson, J. P., Rosales-Ortega, F. F., et al. 2016a, MNRAS, 455, 4087

Galbany, L., Anderson, J. P., Sánchez, S. F., et al. 2018, ApJ, 855, 107

Galbany, L., Hamuy, M., Phillips, M. M., et al. 2016b, AJ, 151, 33

Galbany, L., Stanishev, V., Mourão, A. M., et al. 2014, A&A, 572, A38

Galbany, L., Stanishev, V., Mourão, A. M., et al. 2016c, A&A, 591, A48

Gal-Yam, A., Arcavi, I., Ofek, E. O., et al. 2014, Natur, 509, 471

Gehrels, N., Chincarini, G., Giommi, P., et al. 2004, ApJ, 611, 1005

Grassberg, E. K., Imshennik, V. S., & Nadyozhin, D. K. 1971, Ap&SS, 10, 28 Gutiérrez, C. P., Anderson, J. P., Hamuy, M., et al. 2014, ApJL, 786, L15

Gutiérrez, C. P., Anderson, J. P., Hamuy, M., et al. 2017, ApJ, 850, 89

```
Hack, W. J., Dencheva, N., Fruchter, A. S., et al. 2012, AAS Meeting, 220,
  135.15
Harris, W. E. 2018, AJ, 156, 296
Hosseinzadeh, G., Valenti, S., McCully, C., et al. 2018, ApJ, 861, 63
Hsiao, E. Y., Phillips, M. M., Marion, G. H., et al. 2019, PASP, 131, 014002
Huchra, J. P., Vogeley, M. S., & Geller, M. J. 1999, ApJS, 121, 287
Inserra, C., Turatto, M., Pastorello, A., et al. 2011, MNRAS, 417, 261
Khazov, D., Yaron, O., Gal-Yam, A., et al. 2016, ApJ, 818, 3
Kilpatrick, C. D., & Foley, R. J. 2018, MNRAS, 481, 2536
Kochanek, C. S., Fraser, M., Adams, S. M., et al. 2017, MNRAS, 467, 3347
Kochanek, C. S., Khan, R., & Dai, X. 2012, ApJ, 759, 20
Kuncarayakti, H., Doi, M., Aldering, G., et al. 2013, AJ, 146, 31
Li, W., Leaman, J., Chornock, R., et al. 2011, MNRAS, 412, 1441
Li, W., Wang, X., van Dyk, S. D., et al. 2007, ApJ, 661, 1013
Liu, Q. Z., Hu, J. Y., Hang, H. R., et al. 2000, A&AS, 144, 219
López-Sánchez, Á. R., Dopita, M. A., Kewley, L. J., et al. 2012, MNRAS,
   426, 2630
Margutti, R., Milisavljevic, D., Soderberg, A. M., et al. 2014, ApJ, 780, 21
Mattila, S., Smartt, S. J., Eldridge, J. J., et al. 2008, ApJL, 688, L91
Mauerhan, J. C., Smith, N., Filippenko, A. V., et al. 2013, MNRAS, 430, 1801
Mauerhan, J. C., van Dyk, S. D., Johansson, J., et al. 2017, ApJ, 834, 118
Maund, J. R., Fraser, M., Smartt, S. J., et al. 2013, MNRAS, 431, L102
Maund, J. R., Reilly, E., & Mattila, S. 2014, MNRAS, 438, 938
Maund, J. R., & Smartt, S. J. 2005, MNRAS, 360, 288
Maund, J. R., & Smartt, S. J. 2009, Sci, 324, 486
Moriya, T. J., Pruzhinskaya, M. V., Ergon, M., & Blinnikov, S. I. 2016,
   MNRAS, 455, 423
Morozova, V., Piro, A. L., & Valenti, S. 2017, ApJ, 838, 28
Morozova, V., Piro, A. L., & Valenti, S. 2018, ApJ, 858, 15
Osterbrock, D. E., & Ferland, G. J. 2006, Astrophysics of Gaseous Nebulae
   and Active Galactic Nuclei (Sausalito, CA: University Science Books)
Pastorello, A., Cappellaro, E., Inserra, C., et al. 2013, ApJ, 767, 1
Patat, F., Barbon, R., Cappellaro, E., & Turatto, M. 1993, A&AS, 98, 443
Patat, F., Barbon, R., Cappellaro, E., & Turatto, M. 1994, A&A, 282, 731
Paxton, B., Bildsten, L., Dotter, A., et al. 2011, ApJS, 192, 3
Paxton, B., Cantiello, M., Arras, P., et al. 2013, ApJS, 208, 4
Paxton, B., Marchant, P., Schwab, J., et al. 2015, ApJS, 220, 15
Pettini, M., & Pagel, B. E. J. 2004, MNRAS, 348, L59
Pols, O. R., Tout, C. A., Eggleton, P. P., & Han, Z. 1995, MNRAS, 274,
Poznanski, D., Prochaska, J. X., & Bloom, J. S. 2012, MNRAS, 426, 1465
Pozzo, M., Meikle, W. P. S., Fassia, A., et al. 2004, MNRAS, 352, 457
Prabhu, T. P., & Anupama, G. C. 2010, in ASI Conf. Ser. 1, Interstellar Matter
   and Star Formation: A Multi-wavelength Perspective, ed. D. K. Ojha, 193
Quimby, R., Höflich, P., Kannappan, S. J., et al. 2006, ApJ, 636, 400
Roming, P. W. A., Kennedy, T. E., Mason, K. O., et al. 2005, SSRv, 120, 95
Sagar, R. 1999, CSci, 77, 643
```

```
Sagar, R., Kumar, B., Omar, A., & Pandey, A. K. 2012, Proc. SPIE, 8444,
Sana, H., de Mink, S. E., de Koter, A., et al. 2012, Sci, 337, 444
Sánchez, S. F., Rosales-Ortega, F. F., Marino, R. A., et al. 2012, A&A,
  546, A2
Schady, P., Eldridge, J. J., Anderson, J., et al. 2019, MNRAS, 490, 4515
Schlafly, E. F., & Finkbeiner, D. P. 2011, ApJ, 737, 103
Schlegel, E. M. 1996, AJ, 111, 1660
Smartt, S. J. 2009, ARA&A, 47, 63
Smartt, S. J., Maund, J. R., Hendry, M. A., et al. 2004, Sci, 303, 499
Smith, N. 2014, ARA&A, 52, 487
Smith, N., Cenko, S. B., Butler, N., et al. 2012, MNRAS, 420, 1135
Smith, N., Mauerhan, J. C., Cenko, S. B., et al. 2015, MNRAS, 449, 1876
Spiro, S., Pastorello, A., Pumo, M. L., et al. 2014, MNRAS, 439, 2873
Stetson, P. B. 1987, PASP, 99, 191
Szalai, T., Vinkó, J., Könyves-Tóth, R., et al. 2019, ApJ, 876, 19
Tartaglia, L., Sand, D. J., Valenti, S., et al. 2018, ApJ, 853, 62
Terreran, G., Jerkstrand, A., Benetti, S., et al. 2016, MNRAS, 462, 137
The Astropy Collaboration, Price-Whelan, A. M., Sipőcz, B. M., et al. 2018,
   ApJ, 156, 123
Tomasella, L., Cappellaro, E., Fraser, M., et al. 2013, MNRAS, 434, 1636
Tsvetkov, D. Y. 1983, PZ, 22, 39
Tully, R. B., Shaya, E. J., Karachentsev, I. D., et al. 2008, ApJ, 676, 184
Vacca, W. D., Cushing, M. C., & Rayner, J. T. 2003, PASP, 115, 389
Valenti, S., Benetti, S., Cappellaro, E., et al. 2008, MNRAS, 383, 1485
Valenti, S., Howell, D. A., Stritzinger, M. D., et al. 2016, MNRAS, 459,
Valenti, S., Sand, D., Pastorello, A., et al. 2014, MNRAS, 438, L101
Valenti, S., Sand, D., Stritzinger, M., et al. 2015, MNRAS, 448, 2608
Valenti, S., Sand, D. J., & Wyatt, S. 2018, TNSTR, 1816, https://wis-tns.
  weizmann.ac.il/object/2018ivc/discovery-cert
van Dyk, S. D. 2017, RSPTA, 375, 20160277
van Dyk, S. D., Zheng, W., Maund, J. R., et al. 2019, ApJ, 875, 136
Weilbacher, P. M., Streicher, O., Urrutia, T., et al. 2014, in ASP Conf. Ser.
  485, The MUSE Data Reduction Pipeline: Status after Preliminary
   Acceptance Europe, ed. N. Manset & P. Forshay (San Francisco, CA:
  ASP), 451
Williams, G. G., Milne, P. A., Park, H. S., et al. 2008, in AIP Conf. Ser. 1000,
  Gamm-ray Bursts 2007, ed. M. Galassi, D. Palmer, & E. Fenimore
  (Melville, NY: AIP), 535
Wilms, J., Allen, A., & McCray, R. 2000, ApJ, 542, 914
Wright, D. E., Smartt, S. J., Smith, K. W., et al. 2015, MNRAS, 449, 451
Yang, S., Sand, D. J., Valenti, S., et al. 2019, ApJ, 875, 59
Yang, S., Valenti, S., Cappellaro, E., et al. 2017, ApJL, 851, L48
Yaron, O., & Gal-Yam, A. 2012, PASP, 124, 668
Young, T. R., & Branch, D. 1989, ApJL, 342, L79
Zhang, X., Zhang, J., Wang, X., et al. 2018, ATel, 12240, 1
```